

DEBRIS DISPERSAL FROM REACTOR CAVITIES DURING HIGH-PRESSURE MELT EJECTION ACCIDENT SCENARIOS

N.K. Tutu, T. Ginsberg, C. Finrock,
J. Klages, and C.E. Schwarz

July 1988

DEPARTMENT OF NUCLEAR ENERGY, BROOKHAVEN NATIONAL LABORATORY
UPTON, LONG ISLAND, NEW YORK *1973



Prepared for
United States Nuclear Regulatory Commission
Office of Nuclear Regulatory Research
Washington, D.C. 20555
Under Contract No. DE-AC02-76CH00016

8811070088 880731
PDR NUREG
CR-5146 R PDR

DEBRIS DISPERSAL FROM REACTOR CAVITIES DURING HIGH-PRESSURE MELT EJECTION ACCIDENT SCENARIOS

N.K. Tutu, T. Ginsberg, C. Finrock,
J. Klages, and C.E. Schwarz

Manuscript Completed — September 1987
Date Published — July 1988

EXPERIMENTAL MODELING GROUP
DEPARTMENT OF NUCLEAR ENERGY
BROOKHAVEN NATIONAL LABORATORY
UPTON, LONG ISLAND, NEW YORK 11973

Prepared for
UNITED STATES NUCLEAR REGULATORY COMMISSION
OFFICE OF NUCLEAR REGULATORY RESEARCH
WASHINGTON, D.C. 20555
UNDER CONTRACT NO. DE-AC02-76CH00016
FIN A-3024

ABSTRACT

This report presents the results of a scoping experimental study of the "extent of molten debris dispersal" from PWR reactor cavities under direct containment heating conditions. Simulated high-pressure melt ejection experiments were conducted using 1/42nd-scale models of reactor cavities and were designed to employ low-temperature melt simulants. Three "representative" reactor cavities were selected: Zion, Surry, and Watts Bar. A scaling analysis of the debris dispersal phenomena was carried out and was employed to extrapolate the experimental results for "debris dispersal fraction" to accident conditions. The experimental results, along with the interpretation based upon the scaling analysis, suggest that the three reactor cavities studied here, i.e., Zion, Surry, and Watts Bar, would retain little, if any, of the melt ejected into them from the reactor vessel following the high-pressure steam blowdown which would follow vessel failure and melt release.

TABLE OF CONTENTS

	<u>Page</u>
ABSTRACT	iii
LIST OF FIGURES	vi
LIST OF TABLES	vii
ACKNOWLEDGMENTS	ix
NOMENCLATURE	xi
EXECUTIVE SUMMARY	1
1. INTRODUCTION	5
2. SCALING OF DEBRIS DISPERSAL PHENOMENA	9
2.1 Scaling Methodology and a Simple Idealized Model of the Cavity Melt Dispersal Process	9
2.2 One-Dimensional Conservation Equations	11
2.3 Modeling of F_{GL}^i and r_w	13
2.4 Modeling of Volumetric Gas-Liquid Heat Transfer Rate, \dot{q}	15
2.5 Derivation of the Scaling Parameters	17
2.6 Physical Interpretation of Dimensionless Parameters	26
3. EXPERIMENTAL SIMULATION OF MELT DISPERSAL FROM REACTOR CAVITIES ...	29
3.1 Selection of Plant-Specific Reactor Cavities	29
3.2 Selection of Accident Initial Conditions	29
3.3 Experimental Method and Parameters	33
4. EXPERIMENTAL RESULTS	43
4.1 Results for the Zion Reactor Cavity Model	43
4.2 Results for the Surry Reactor Cavity Model	43
4.3 Results for the Watts Bar Reactor Cavity Model	47
5. DISCUSSION AND SCALING INTERPRETATION OF DISPERSAL RESULTS	53
5.1 Qualitative Effect of Dimensionless Groups on Debris Dispersal	53
5.2 Discussion of Dispersal Results for the Zion Cavity	54
5.3 Discussion of Dispersal Results for the Surry Cavity	54
5.4 Discussion of Dispersal Results for the Watts Bar Cavity	55
6. SUMMARY AND CONCLUSIONS	57
REFERENCES	61

LIST OF FIGURES

	<u>Page</u>
1. Schematic of High-Pressure Melt Ejection and the Direct Containment Heating Accident Scenario	6
2. Schematic of "Model" Flow Regime	13
3. Schematic of Experimental Setup	34
4. Photograph of the Experimental Facility Showing a Model of the Watts Bar Cavity Under Test	35
5. (a) Photograph of the Zion Reactor Cavity Model	36
5. (b) Photograph of the Surry Reactor Cavity Model	37
5. (c) Photograph of the Watts Bar Reactor Cavity Model	38
6. (a) Schematic of the Zion Cavity Model.....	39
6. (b) Schematic of the Surry Cavity Model	40
6. (c) Schematic of the Watts Bar Cavity Model	41
7. Schematic of Observed Gas Flow Field Within the Zion Cavity	45
8. Trapped Wood's Metal in the Surry Cavity Model at the End of Run S-4	48
9. Schematic of Observed Gas Flow Field Within the Surry Cavity	49
10. Melt Deposition Within the Watts Bar Cavity at the End of Run WB-7	51
11. Schematic of the Observed Gas Flow Field Within the Watts Bar Cavity	52

LIST OF TABLES

	<u>Page</u>
1. Reference Values for Various Variables	19
2. Similarity Parameters for the Debris Dispersal Process	25
3. Summary of IDCOR Reactor Cavity Configurations	30
4. Initial Conditions for the Full-Scale Reactor Cavities	31
5. Experimental Parameters for Debris Dispersal Tests	42
6. Results of Debris Dispersal Experiments and the Values of Various Dimensionless Groups for the Zion Cavity Model	44
7. Results of Debris Dispersal Experiments and the Values of Various Dimensionless Groups for the Surry Cavity Model	46
8. Results of Debris Dispersal Experiments and the Values of Various Dimensionless Groups for the Watts Bar Cavity Model	50

ACKNOWLEDGMENTS

The authors gratefully acknowledge the work of K. Becker in the preparation of this report for publication.

This work was performed under contract to the United States Nuclear Regulatory Commission, Office of Nuclear Regulatory Research, Division of Accident Evaluation, Containment Systems Branch. The authors acknowledge the support of Dr. T. M. Lee during the course of the investigation.

NOMENCLATURE

A	Cross-sectional area of the duct (or cavity)
A_R	Cross-sectional area of the duct (or cavity) at a specified location
A_t	Cross-sectional area of the hole in the pressure vessel bottom during the steam (or gas) blowdown phase
c	Speed of sound for the gas phase
C_D	Drag coefficient for liquid droplets
c_p	Specific heat at constant pressure for the gas phase
c_R	Reference value of the sonic speed for the gas phase (see Table 1)
c_v	Specific heat at constant volume for the gas phase
D	Hydraulic diameter
d	Droplet diameter
E_i	Liquid mass entrainment rate per unit wall area of the duct
F_{gL}^1	Interfacial drag on the liquid phase due to gas phase per unit volume of the duct (or cavity) = $(F_{gL}^1)_1 + (F_{gL}^1)_2$
$(F_{gL}^1)_1$	Interfacial drag on the liquid film due to the gas phase per unit volume of the duct
$(F_{gL}^1)_2$	Interfacial drag on the liquid droplets due to the gas phase per unit volume of the duct
f_i	Friction factor
f_s	Single phase smooth pipe friction factor
$f(\gamma)$	See Equation (27)
g_x	Component of acceleration due to gravity along the x direction
h	Heat transfer coefficient
j_g	Superficial velocity of the gas phase

i_L	Superficial velocity of the liquid phase
k_g	Thermal conductivity of the gas phase
L	Length scale of the cavity
M_0	Total mass of steam (or gas) in the primary system at $t = 0$ (instant of the beginning of steam blowdown)
m	Thickness of liquid film along the walls of the duct (or cavity)
\dot{m}_g	Instantaneous mass flow rate of steam (or gas) leaving the primary system
\dot{m}_g^0	Steam (or gas) mass flow rate leaving the primary system at $t = 0$
N_1 through N_{12}	Dimensionless numbers (see Table 2)
n	Number of droplets per unit volume of the duct (or cavity)
P	Pressure
P_0	Pressure of gas in the primary system at the instant of vessel failure
P_∞	Containment pressure
\dot{q}	Heat transfer rate from the liquid to the gas phase per unit volume of the duct = $(\dot{q})_1 + (\dot{q})_2$
$(\dot{q})_1$	Heat transfer rate from the liquid film to the gas phase
$(\dot{q})_2$	Heat transfer rate from the liquid droplets to the gas phase
R	Gas constant for the gas phase
Re	Reynolds number of flow around a droplet
S	Perimeter of the duct (or cavity)
s	Entropy of the gas phase
T_g	Temperature of the gas phase
T_L	Temperature of the liquid phase (melt or melt simulant)
T_0	Temperature of steam (or gas) in the primary system at the instant of vessel failure

t	Time, $t = 0$ corresponds to the beginning of the steam (or gas) blowdown from the pressure vessel
t_R	$= L/u_R$, the time scale
u_g	Velocity of the gas phase
u_L	Velocity of the liquid phase
u_R	Reference value of the velocity (see Table 1)
V_0	Volume of steam (or gas) in the primary system
x	Longitudinal coordinate along the one-dimensional duct (or cavity), x increases towards cavity exit

Superscript

- * Dimensionless form of the variable, e.g., D^* ($=D/L$) is the dimensionless hydraulic diameter, see page 18

Greek Symbols

α	Void fraction
β	Volume fraction occupied by liquid droplets
γ	$= c_p/c_v$
μ_g	Absolute viscosity of the gas phase
μ_L	Absolute viscosity of the liquid phase
ρ_g	Density of the gas phase
ρ_L	Density of the liquid phase
ρ_0	Steam (or gas) density in the pressure vessel at the instant of vessel failure
ρ_R	Reference value of the gas density (see Table 1)
σ	Surface tension of the liquid-gas pair
τ_i	Interfacial shear stress on the liquid film
τ_w	Shear stress along the walls of the duct (or cavity)

EXECUTIVE SUMMARY

Consider a potential core melt accident sequence during which the reactor pressure vessel fails while the primary system is still at high pressure. The molten core material, consisting of oxides and unreacted zirconium and stainless steel, is assumed driven from the reactor vessel under high primary system pressure into the region beneath the vessel (reactor cavity). Steam, which follows the melt discharge from the vessel, flows at high velocity through the reactor cavity region, finely fragments the molten core material into droplets, interacts thermally and chemically (thus producing hydrogen) with the melt, and carries some fraction of melt droplets into the containment subcompartments just above the cavity. As the melt flows through the subcompartments, a portion of the suspended droplets will likely be deposited on structures. As the gases (steam and hydrogen) flow around intervening structures to the upper dome region of the containment building, a small fraction of fine core melt debris will also be carried into the upper dome. Hydrogen produced in the reactor cavity and subcompartments will be transported to the dome where combustion with oxygen would occur if conditions permitted. The core debris, during its flight through the subcompartments and the containment dome, transfers some fraction of its thermal and chemical energy directly to the containment atmosphere. This phenomenon of direct energy exchange between the core melt and containment atmosphere (via melt-atmosphere heat transfer, melt-steam chemical reaction, melt-oxygen chemical reaction, and hydrogen combustion), which leads to rapid containment pressurization, is termed direct containment heating (DCH).

The DCH accident sequence involves interactions in three regions of the containment building: (i) the reactor cavity, (ii) the intermediate subcompartments, and (iii) the containment dome. The fraction of melt inventory transported, or "dispersed," from the reactor cavity is believed to have a strong influence on the subsequent stages of the DCH accident sequence. Melt which is retained within the cavity following steam blowdown cannot transfer its remaining inventory of thermal and chemical energy to the containment atmosphere and, therefore, would be effectively removed from further consideration as far as DCH containment loading is concerned. Conversely, melt which is dispersed from the reactor cavity will transfer a fraction of its retained stored energy to the containment atmosphere and must be considered in subsequent loading analysis. If, therefore, there are plants whose reactor cavity designs contain particular structural features that can be shown to lead to negligible melt dispersal by the flowing gases, then the DCH loading for those plants would be minimal. Based upon this point of view there would be clear benefits to identification of plants, or categories of plants, whose cavities could be shown to be capable of retention of large quantities of melt. Thus, it was felt that a scoping experimental effort should be carried out to investigate the "potential for dispersal" of melt from several "representative" reactor cavity designs.

This report describes and presents the results of a scoping experimental study of the "extent of molten debris dispersal" from PWR reactor cavities under conditions of high-pressure melt ejection (primary system pressure approximately 1000 psia and vessel hole diameter roughly 0.4 m diameter). The experiments were conducted using scale models of the reactor cavities and were

designed to employ low-temperature melt simulants. As a consequence, the experimental program was developed in conjunction with a parallel scaling analysis which is based upon phenomenological modeling of the relevant physical processes which are thought to occur within a full-scale reactor cavity under accident conditions. The experimental apparatus and method are described and experimental results presented. The phenomenological modeling and the derivation of the scaling relationships are described. A methodology based upon the scaling analysis is presented which is employed to extrapolate the experimental results for the "debris dispersal fraction" to accident conditions.

Three "representative" reactor cavities were selected: Zion, Surry and Watts Bar. An experimental apparatus was constructed to simulate the process of melt dispersal from reactor cavities during high-pressure melt ejection. The cavities were constructed to provide 1/42-nd scale simulations of the prototypic cavities and were fabricated of transparent materials to enable visual observations to be made of the flow processes within the cavities. Water and Wood's metal were employed as the low-temperature melt simulants while nitrogen and helium were used to simulate the high-pressure primary system steam (prototypic) blowdown gas. A measured quantity of melt simulant, followed immediately by blowdown gas, was injected into the cavity. The quantity of melt remaining in the cavity following the gas blowdown was measured, thus permitting calculation of the "fraction of melt dispersed" from the cavity for the given set of initial conditions. High-speed motion pictures of the cavity dispersal phenomena were recorded, from which flow patterns within the cavity were deduced.

The high-speed movies of the cavity interactions reveal a complex, multi-dimensional dispersed flow configuration within the cavity models. The melt simulant enters the cavity through an orifice in a jet configuration, whereupon the jet strikes the cavity floor and apparently distributes itself along the walls of the cavity model, all under its own momentum. Gas follows the liquid into the cavity and subsequently appears to entrain and fragment the liquid into droplets, creating a dispersed droplet flow regime within the model. The droplets are transported out of the cavity by the flowing gas.

The above qualitative observations form the conceptual basis for development of the phenomenological model of reactor cavity phenomena. This model is then applied to the scaling analysis from which the scaling relationships are derived. The model presumes the existence of a "dispersed annular-flow" regime within the reactor cavity, where droplets are dispersed in a gas core region and a liquid film is presumed to exist on the walls of the cavity. Eulerian, unsteady, one-dimensional mass, momentum and energy equations are written for each phase. Liquid temperature is assumed constant and chemical reaction between phases is not considered. Simplified constitutive relations for interfacial forces, heat transfer and entrainment are proposed. These equations, together with the appropriate initial and boundary conditions are non-dimensionalized using reference parameters for the basic variables. This process leads to definition of eleven dimensionless parameters which characterize the debris dispersal process in the experiments. A physical interpretation of the parameters is provided in order to guide their use in scaling of the experimental results to prototypic accident conditions.

A range of initial accident conditions is defined for each of the three plants considered and a range of magnitudes of the eleven scaling parameters are calculated for each. It is shown that it is not, in general, possible to precisely match the values of the prototypic and experimental scaling parameters. The experiments reported here are performed at low temperature. As a consequence, the gas phase acceleration effects of droplet-gas heat transfer cannot be precisely simulated. An approximate method of overcoming this difficulty is employed, which relies on the assumption that the melt and steam reach thermal equilibrium very quickly within the cavity. It is further argued, on the basis of physical interpretation of the scaling parameters and with the aid of engineering judgment, that the values of the scaling parameters could be adjusted experimentally so as to provide "melt dispersal fraction" data which underestimate the extent of melt dispersal from full-scale reactor cavities under accident conditions. With the experimental scaling parameters chosen in this way the "melt dispersal fraction" data obtained using Wood's metal as the melt simulant are believed to underestimate the extent of melt dispersal under high-pressure accident conditions. Thus, if an experiment designed to simulate a high-pressure melt ejection accident led to measurement of dispersal of, for example, 80% of the melt injected into the cavity, then the interpretation of this result is that, under accident conditions, greater than 80% of the melt would be ejected from the reactor cavity. Only those experiments which could be interpreted in this way are used for the purpose of estimation of the extent of melt dispersal. For this reason, the water experiments performed here were not used for this purpose.

The experiments performed thus far with the Zion cavity were performed using water as melt simulant. Based upon the above arguments, therefore, we cannot make any judgements of the extent of melt dispersal for this system. It is noted that experiments performed elsewhere [2,3] suggest that melt ejection from the Zion reactor cavity would be nearly complete under conditions of high-pressure melt ejection. This conclusion will be verified in additional planned experiments using Wood's metal as the melt simulant. Experiments with both the Surry and Watts Bar cavities, together with the scaling arguments, suggest that melt dispersal will also be nearly complete (in excess of 80%) under high-pressure melt ejection conditions.

The motion pictures of the flow patterns in the Watts Bar cavity suggest that the high-temperature dispersed melt flows through the cavity and up the inclined keyway where the flow is observed to split into two parts. One of the two resulting flow streams moves towards the seal table where the flow reverses direction and finally exits the cavity. The seal table room is covered with a steel plate which would be exposed to the high-temperature (e.g. 2500K) molten debris. It has been suggested [15] that this cover plate could fail during the time of melt ejection from the cavity, leading to transport of melt into the seal table room where contact of the melt with the containment liner could occur. Meltthrough of this liner would effectively imply a breach of containment and "early" availability of a leakage path for fission products to the atmosphere. It is recommended that the scenario of the seal table cover plate failure during high-pressure melt ejection accidents be closely scrutinized.

The experimental results, along with the interpretation based upon the scaling analysis, suggest that the three reactor cavities studied here, i.e., Zion, Surry and Watts Bar, would retain little, if any, of the melt ejected into them from the reactor vessel following the high-pressure steam blowdown which would follow vessel failure and melt release. It is suggested that these conclusions be verified with experiments at larger scale using high-temperature melt simulant materials.

1. INTRODUCTION

The high-pressure melt ejection, or direct containment heating (DCH), accident scenario influences the nuclear reactor severe accident radiological source term by potentially altering the timing of containment failure and by leading to additional mechanisms which produce radioactive aerosols. Direct containment heating, discussed here in the context of pressurized water reactors (PWRs) is the mechanism of containment loading which results from transfer of thermal and chemical energy from high-temperature, finely-divided molten core material to the containment atmosphere. The DCH accident sequence involves interactions in three regions of the containment building, shown schematically in Figure 1: (i) the reactor cavity, (ii) the intermediate sub-compartments and (iii) the containment dome.

The molten core material, consisting of oxides and unreacted zirconium and stainless steel, is driven from the reactor vessel under high primary system pressure into the region beneath the vessel. Steam, which follows the melt from the vessel, flows at high velocity through the reactor cavity region, finely subdivides the molten core material and carries some fraction of the melt as droplets into the subcompartments just above the reactor cavity. Thermal and chemical transfer interactions occur between the steam and droplets within the cavity and the subcompartments. Hydrogen is produced as the steam reacts with the unreacted molten metallics. As the melt flows through the subcompartments a portion of the suspended droplets will likely be deposited on structures. As the gas flows around intervening structures to the upper dome region of containment, therefore, only a fraction of the molten material which exits the cavity will be carried with it. This material will then interact with the atmosphere in the dome region. Hydrogen produced in the subcompartments and the cavity will be transported to the dome where combustion with oxygen would occur if conditions permitted.

Efforts are under way at Brookhaven National Laboratory (BNL) and at Sandia National Laboratories (SNL) to develop integrated methodologies which will predict the response of containment buildings to the loads imposed by the interactions in the various regions of containment. This report presents the results of an experimental program directed towards describing phenomena which would occur within the reactor cavity during a DCH accident sequence.

The BNL experimental program related to reactor cavity dynamics has both long-term and short-term goals. The long-term goal of the research related to reactor cavity dynamics is to develop a methodology to characterize the thermal, chemical and mechanical interactions which would occur in the cavity. Such a model would characterize: (i) the rate of flow of melt from the reactor cavity to the upper regions of containment, (ii) the melt droplet size distribution and (iii) the extent of hydrogen production within the cavity. The methodology would be capable of dealing with the differences in reactor cavity designs, examples of which are presented later in this report. This work, currently in progress, will provide the transient melt and gas momentum and mass fluxes at the cavity exit during the high-pressure melt ejection and steam blowdown process.

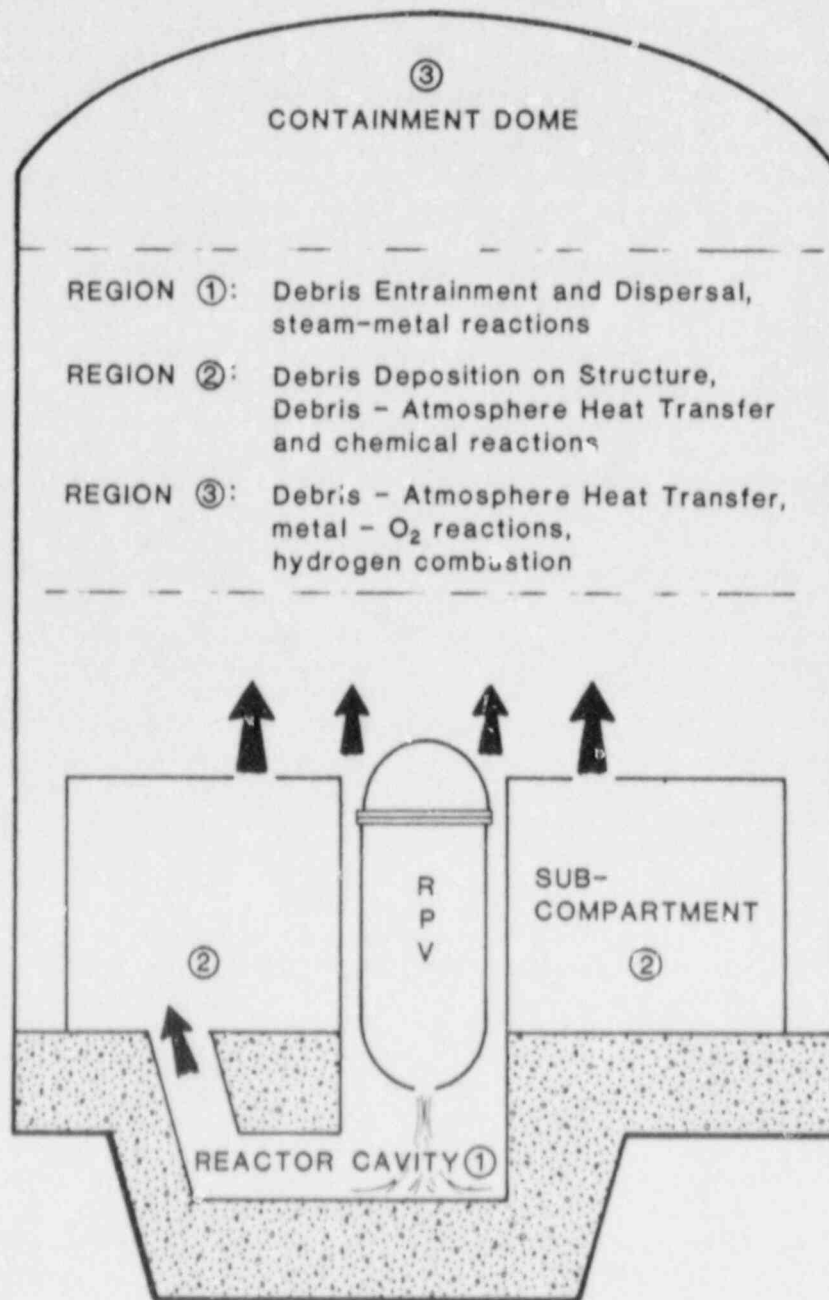


Figure 1 Schematic of High-Pressure Melt Ejection and the Direct Containment Heating Accident Scenario

The fraction of melt inventory transported, or "dispersed," from the reactor cavity is believed to have a strong influence on the subsequent stages of the DCH accident sequence. Melt which is retained within the cavity following steam blowdown cannot transfer its remaining inventory of thermal and chemical energy to the containment atmosphere and, therefore, would be effectively removed from further consideration as far as DCH containment loading is concerned. Conversely, melt which is dispersed from the reactor cavity will transfer a fraction of its retained stored energy to the containment atmosphere and must be considered in subsequent loading analysis. If, therefore, there are plants whose reactor cavity designs contain particular structural features that can be shown to lead to negligible melt dispersal by the flowing gases, then the DCH loading for those plants would be minimal. Based upon this point of view there would be clear benefits to identification of plants, or categories of plants, whose cavities could be shown to be capable of retention of large quantities of melt. Thus, it was felt that a scoping experimental effort should be carried out to investigate the "potential for dispersal" of melt from several "representative" reactor cavity designs.

Based upon the above considerations the short-term goal of the BNL experimental program was defined: to determine the "extent of debris dispersal" from PWR reactor cavities of various "representative" designs. Three reactor cavity designs were selected: Zion, Surry and Watts-Bar. The reasons for their selection are discussed in Chapter 3. The objectives of this report are: (i) to describe the experimental program, (ii) to present the experimental results and, (iii) to provide an interpretation of the results using a scaling analysis which is based upon phenomenological modeling of the relevant physical processes.

Experiments related to debris dispersal from scale models of the Zion reactor cavity were performed at Argonne National Laboratory [1,2] and at Sandia National Laboratories [3]. Spencer et al. [1], using a 1/40-th linear (all references to scale will imply linear scaling in this report) scale model and simulant fluids, demonstrated that a threshold gas velocity within the cavity must be exceeded in order to disperse liquid from the reactor cavity. Tarbell et al. [3] performed high pressure debris dispersal experiments using a 1/10-th scale concrete model of the Zion reactor cavity using iron-alumina thermite. These experiments demonstrated nearly complete dispersal of melt from the Zion cavity model.

For reasons of economy the BNL cavity dispersal experiments are, as were the ANL and SNL experiments, constrained to scales (1/42-nd) which are much smaller than prototypic scale. In addition, the BNL experiments are designed to use melt simulants at low (near ambient) temperatures. Therefore, a scaling analysis must be performed both to allow suitable choice of the experimental parameters and to permit extrapolation of results as they would apply to actual full-scale accident conditions. A detailed scaling analysis of debris dispersal phenomena is presented in this report. The results of the experiments are discussed with the aid of this scaling analysis.

The scaling analysis of debris dispersal phenomena is presented in Chapter 2. The choice of the specific reactor cavities used in the experiments is discussed in Chapter 3 along with the description of the experimental apparatus and methods. Chapter 4 presents the results of the experimental effort. A discussion of the experimental results is presented in Chapter 5. The summary and conclusions are presented in Chapter 6.

2. SCALING OF DEBRIS DISPERSAL PHENOMENA

2.1 Scaling Methodology and a Simple Idealized Model of the Cavity Melt Dispersal Process

As mentioned in the last chapter, the short-term goal of our experiments is to determine the extent of melt dispersal for various reactor cavity designs during a high-pressure melt ejection accident sequence. Consequently, the scaling analysis presented here is focused on the debris dispersal phenomena only. Moreover, the analysis assumes that the initial conditions, i.e., the mass and temperature of the molten core material, the primary system pressure, P_0 , at vessel failure, the size of the hole in the reactor pressure vessel bottom at the beginning of the steam blowdown, the containment pressure P_∞ , are known or given.

Before discussing the scaling procedure, let us first look at some of the important phenomena that will occur in the actual reactor cavities during a high-pressure melt ejection accident sequence, and that our experiments are not designed to simulate. The thermal interaction of the high temperature core-melt with the concrete surface of the reactor cavity is likely to result in the generation of steam and carbon dioxide gases at the melt-concrete interface due to the disintegration of concrete. As a result, the melt layer or film on the cavity surface is likely to be blown away from the surface. This local gas production on the cavity surface will then cease until the whole cycle is begun once again due to the rewetting of the surface. It is easy to see that, due to this melt-concrete interaction, the melt is unlikely to freeze on the concrete cavity walls during the short duration of the steam blowdown from the pressure vessel. That freezing of core melt in a concrete cavity is unlikely to occur is supported by the experiments of Tarbell et al. [3]. They measured 99% of the high temperature melt inventory to exit the 1/10th-scale concrete model of the Zion cavity during a high-pressure melt ejection experiment. By pre-heating the cavity model to a temperature above the melting point of the melt simulant, our experiments easily prevent freezing of the melt simulant on the cavity walls. However, our low temperature experiments are not designed to simulate the intermittent gas production along the cavity walls. Since this gas production can only lead to increased melt entrainment and hence increased debris dispersal, this implies that our experiments will show a lower melt dispersal rate than an experiment which simulated the gas production due to core-concrete thermal interactions.

The second phenomenon that our experiments are not designed to simulate is the metal (zirconium, stainless steel)-steam reaction within the reactor cavity. Since this reaction results in the consumption of high density steam and its replacement by the low density hydrogen, the average density of the flowing gases within the cavity is reduced. For example, if two-thirds of the steam is consumed locally at any point within the cavity (partial pressure of steam equals half the partial pressure of hydrogen), the local density of the steam-hydrogen mixture would be only about 40% of the density of pure steam. Since both the melt entrainment rate and the drag on melt droplets due to the flowing mixture of gases is dependent upon the density of the gas phase, the debris dispersal rate is clearly going to be dependent upon the extent of

steam-metal reaction. Although our experiments are not intended to simulate the local variations in gas density within the cavity due to metal-steam chemical reaction, the experiments can simulate the effect of the net average reduction in the gas density. This, for example, can be done by using a low density driver gas (helium) and reducing the mass flow rate of the gas through the cavity during the experiment.

In view of the above discussion, it is clear that our debris dispersal experiments do not simulate all the phenomena occurring within the reactor cavity. It is important to keep in mind the implications of this. Strictly speaking, our experiments simulate debris dispersal for a "fictitious" full-scale accident scenario* wherein the melt neither interacts thermally with the cavity walls nor does it react chemically with steam. So, it should be remembered that whenever we talk of extrapolating our experimental results to the "full scale," we mean extrapolating to this "fictitious" full-scale accident scenario. When trying to use these results for the actual full-scale case wherein both the core-concrete interaction and metal-steam reactions are operative, the reader must obviously use his judgment. This, as indicated by the above discussion, is not a difficult task if one is only interested in the gross nature of debris dispersal.

One straightforward procedure for determining the scaling parameters is the method of "Dimensional Analysis," which is based upon the use of Buckingham's Pi theorem. This approach was used in the beginning of the experimental program and the results are presented elsewhere [4]. Here, however, we shall present an alternative procedure for determining the dimensionless parameters. The method [5], which is based upon the use of conservation equations describing the phenomena under study, is as follows: Reference values are selected for all the variables, and these values are then used to rewrite all the conservation equations and boundary conditions** in terms of dimensionless variables. The constant coefficients appearing in these equations (or any independent combination of these) are then the parameters that must be kept identical between the small-scale experiments and the full-scale case for "perfect" scaling of experiments.

The following physical model is envisioned for the melt dispersal process within the reactor cavity: As the melt is discharged under high pressure from the pressure vessel, it spreads along the walls of the cavity as a film. When steam blowdown begins, melt droplets are entrained from the film into the central core of gas flow. An assumption about the melt dispersal process is necessary for the purposes of modeling the interfacial gas-liquid drag and wall shear stress terms in the conservation equations. Furthermore, it is also assumed that the melt-steam flow in the reactor cavity is a one-dimensional, transient, two-phase, gas-liquid flow with no mass transfer and chemical reaction between phases.

*In addition, for the present series of experiments, we have neglected the presence of structure (instrument tubes and support plates) within the cavity. It is assumed that this structure fails immediately after or during the melt ejection phase of the accident. Other restrictions are discussed in Chapter 3.

**Initial conditions are viewed as generalized boundary conditions for the time variable.

Section 2.2 describes the development of the basic conservation equations for the gas and liquid phases. The constitutive relations for momentum and heat transfer are described in Sections 2.3 and 2.4. Section 2.5 presents the derivation of the scaling parameters.

2.2 One-Dimensional Conservation Equations

Consider an unsteady one-dimensional flow of gas-liquid mixture through a variable area duct. Then, the continuity equations for the gas and liquid phases are given by:

$$\frac{\partial}{\partial t} (\alpha \rho_g) + \frac{\partial}{\partial x} (\rho_g j_g) + \frac{\rho_g j_g}{A} \frac{dA}{dx} = 0 \quad (1)$$

$$\frac{\partial}{\partial t} (1-\alpha) + \frac{\partial j_L}{\partial x} + \frac{j_L}{A} \frac{dA}{dx} = 0 \quad (2)$$

where j_g and j_L are the gas and liquid superficial velocities, ρ_g is the density of the gas phase, α is the void fraction, A is the cross-sectional area of the duct, x is the longitudinal coordinate along the duct and t is the time. Conservation of linear momentum across an infinitesimal cross section of the duct yields the following momentum equations for the gas and liquid phases:

$$\rho_g \frac{\partial j_g}{\partial t} - \frac{\rho_g j_g}{\alpha} \frac{\partial \alpha}{\partial t} + \rho_g j_g \frac{\partial}{\partial x} \left(\frac{j_g}{\alpha} \right) + F_{gL}^i - \alpha \rho_g g_x + \alpha \frac{\partial P}{\partial x} = 0 \quad (3)$$

$$\rho_L \frac{\partial j_L}{\partial t} - \frac{\rho_L j_L}{(1-\alpha)} \frac{\partial (1-\alpha)}{\partial t} + \rho_L j_L \frac{\partial}{\partial x} \left(\frac{j_L}{(1-\alpha)} \right) + (1-\alpha) \frac{\partial P}{\partial x} - (1-\alpha) \rho_L g_x - F_{gL}^i + \frac{\tau_w S}{A} = 0 \quad (4)$$

where ρ_L is the density of the liquid phase (assumed constant), P is the pressure, g_x is the component of gravitational acceleration along the x direction, τ_w is the shear stress along the walls of the duct, S is the duct perimeter, and F_{gL}^i is the interfacial drag on the liquid phase due to the gas phase per unit volume of the duct. As mentioned in last section, the above equations assume that there is a liquid film along the walls of the duct.

The gas (steam in the full-scale reactor case) is assumed to behave like a perfect gas with constant specific heats. Thus the equation of state is given by:

$$P = \rho_g R T_g \quad (5)$$

where R is the gas constant and T_g is the gas temperature. The energy balance for the gas phase together with the use of gas momentum equation gives:

$$\frac{\gamma \partial T_g}{\partial t} + \frac{\gamma j_g}{a} \frac{\partial T_g}{\partial x} - \frac{1}{\rho_g c_v} \left\{ \frac{\partial P}{\partial t} + \frac{j_g}{a} \frac{\partial P}{\partial x} \right\} - \frac{RT_g}{ac_v} \frac{\partial a}{\partial t} + \frac{g_x j_g}{ac_v} - \frac{F_{GL}^i j_g}{c_v \rho_g a^2} = \frac{\dot{q}}{ac_v \rho_g} \quad (6)$$

where γ is the specific heat ratio for the gas phase, c_v is the specific heat at constant volume for the gas phase, and \dot{q} is the heat transfer rate from the liquid to the gas phase per unit volume of the duct.

For a perfect gas, we can write the following thermodynamic relations:

$$\text{(Gibbs Equation): } dT_g = \frac{T_g}{c_p} ds + \frac{1}{\rho c_p} dP \quad (7)$$

$$d\rho = \frac{dP}{c^2} - \frac{\rho}{c} ds \quad (8)$$

where s is the entropy, c_p is the specific heat at constant pressure and c is the sonic speed. Following Moody [5], using Equations (6), (7), and (8), the continuity equation for the gas phase (1), can be rewritten as:

$$\begin{aligned} \frac{\partial P}{\partial t} + \frac{j_g}{a} \frac{\partial P}{\partial x} - \frac{\dot{q} c^2}{ac_p T_g} + \frac{\rho_g c^2}{a\gamma} \frac{\partial a}{\partial t} + \frac{\rho_g j_g c^2 g_x}{ac_p T_g} - \frac{c^2 F_{GL}^i j_g}{T_g a^2 c_p} \\ + \frac{\rho_g c^2}{a} \frac{\partial j_g}{\partial x} + \frac{\rho_g j_g c^2}{aA} \frac{dA}{dx} = 0 \end{aligned} \quad (9)$$

The reason for the above manipulation is to have the sonic speed appear explicitly in one of the governing equations, so that the Mach number would appear as one of the dimensionless numbers. Before we can use the above set of equations for scaling purposes, we must model the interfacial gas-liquid drag term F_{GL}^i , the wall shear stresses τ_w , and the gas-liquid volumetric heat transfer rate \dot{q} .

2.3 Modeling of F_{gL}^i and τ_w

Figure 2 shows our assumed conceptual picture of flow regime within the duct for the purpose of modeling the interfacial drag term and the wall shear. We split the interfacial gas-liquid drag term, F_{gL}^i , into two components: (i) the drag on the annular liquid film due to the gas phase alone, $(F_{gL}^i)_1$ and (ii) the drag on the liquid droplets due to the gas, $(F_{gL}^i)_2$. Following Wallis [6] and Hewitt [7] we model the interfacial shear stress on the liquid film, τ_i , as:

$$\tau_i = \frac{1}{2} f_i \rho_g \frac{j_g^2}{a^2} \quad (10)^*$$

where the friction factor f_i is given in terms of the single phase smooth pipe friction factor, f_s , the film thickness m , and the hydraulic pipe diameter, D as:

$$f_i = f_s \left[1 + \frac{360 m}{D} \right] \quad (11)$$

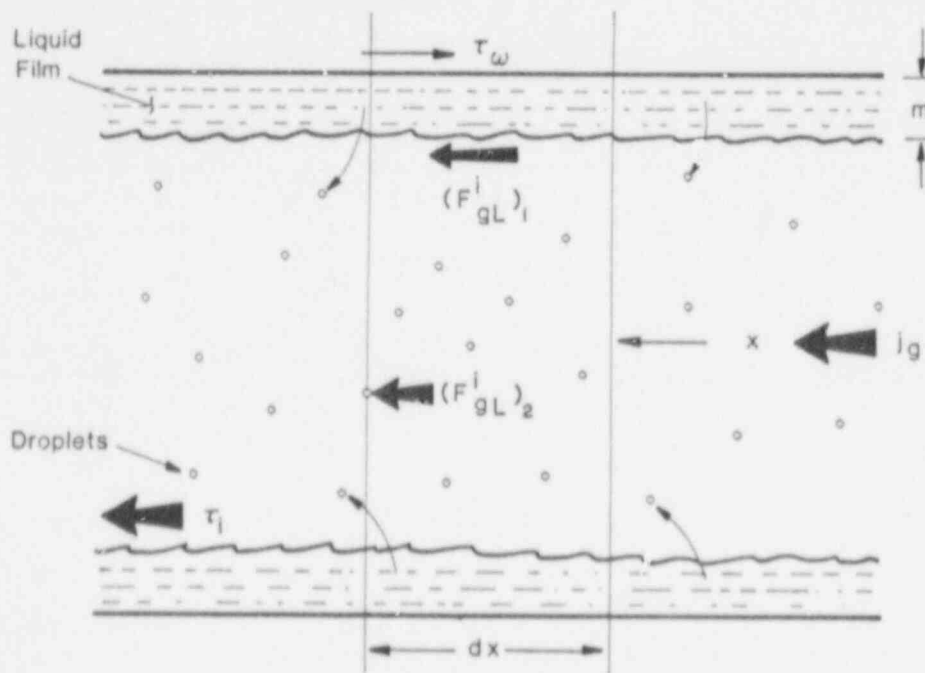


Figure 2 Schematic of "Model" Flow Regime

*The actual model proposed by Hewitt [7] uses a "mixture" density of the gas core (instead of ρ_g) in this equation.

It then follows that

$$(F_{gL}^1)_1 = \frac{\tau_1^4}{D} = \frac{2}{Da^2} f_1 \rho_g j_g^2 \quad (17)$$

To model $(F_{gL}^1)_2$, we must first calculate the number of droplets per unit volume in the gas core and the size of these droplets. A critical Weber number of 12 is assumed to give us the droplet diameter, d [8]. Thus,

$$d = \frac{12 \sigma}{\rho_g u_g^2 (1 - u_L/u_g)^2} \quad (13)$$

Based on the entrainment data presented by Hewitt [7], which shows the dimensionless entrainment rate asymptotically approaching 10 as the dimensionless number τ_{1m}/σ approaches 1, we model the liquid mass entrainment rate per unit wall area of the duct, E_1 as:

$$E_1 = 10 \tau_{1m}/\sigma = \frac{5 \mu_L f_1 \rho_g j_g^2}{\sigma \alpha^2} \quad (14)$$

where μ_L is the absolute viscosity of the liquid and σ is the surface tension of the liquid-gas pair. Here we note that, for the debris dispersal problem that we are considering, calculations show that $\tau_{1m}/\sigma \gg 1$, and that [7] does not present any entrainment data in this range. Since we are neglecting the deposition of droplets on the liquid film, the above model for the entrainment rate should be viewed as a model for the net entrainment rate (entrainment rate minus the deposition rate). To find an expression for the mass of liquid droplets per unit volume at any position x within the duct, we assume a quasi-steady flow and integrate the following conservation equation for the droplet field mass.

$$\frac{d}{dx} (\rho_L A \beta u_L) = E_1 S$$

where β is the volume fraction occupied by the liquid droplets. It is assumed that $\beta = 0$ at $x = 0$. Equation (13) is then used to find the number of liquid droplets per unit volume of the duct. By adding the drag on all liquid droplets within a unit volume it is then possible to find an expression for $(F_{gL}^1)_2$ as:

$$(F_{gL}^i)_2 = \frac{5}{4} C_D \frac{u_L \rho_g^2 j_g^3 (1-u_L/u_g)^4}{\alpha^3 \rho_L \sigma^2 (u_L/u_g)} \frac{x}{D} \left[\frac{f_1 \rho_g j_g^2}{\alpha^2} \right]_{x=x_m}$$

where u_L and u_g are the velocities of the liquid and gas phases respectively, C_D is the drag coefficient experienced by a liquid droplet, and x_m ($0 \leq x_m \leq x$) is the location at which the quantity within square brackets above is equal to the average value between zero and x . In view of the uncertainty in Equation (14), and also since our intent here is only to use the model equations for determining the scaling parameters, we shall, for the sake of simplicity, assume $x_m = x$. Thus, we model $(F_{gL}^i)_2$ as:

$$(F_{gL}^i)_2 = C_D f_1 \frac{u_L \rho_g^3 j_g^5 (1-u_L/u_g)^4}{\alpha^5 \sigma^2 \rho_L (u_L/u_g)} \frac{x}{D} \quad (15)$$

The total gas-liquid interfacial drag F_{gL}^i is given by

$$F_{gL}^i = (F_{gL}^i)_1 + (F_{gL}^i)_2 \quad (16)$$

At the high gas velocities that are likely to be present in the reactor cavity region during the high pressure melt ejection accident, we expect most of the debris dispersal to occur in the form of entrained droplets. Thus the acceleration of the liquid film is not very critical to correctly calculating the amount of debris dispersed. Since the wall shear stress τ_w only affects the motion of the liquid film, its modeling can therefore be relatively crude. We use the following model which assumes constant shear stress in the liquid film.

$$\tau_w = \frac{2u_L j_L}{(1-\alpha)m} \quad (17)$$

2.4 Modeling of Volumetric Gas-Liquid Heat Transfer Rate, \dot{q}

Analogous to the modeling of gas-liquid interfacial drag F_{gL}^i , we divide the gas-liquid heat transfer rate into two components: (1) the q_{GL}^i heat transfer

from the liquid film to the gas, $(\dot{q})_1$ and (ii) the heat transfer from the liquid droplets to the gas, $(\dot{q})_2$. To evaluate the former, we use Reynold's Analogy [9] and assume that the heat transfer coefficient for pipe flow applies. Thus, the liquid film-gas heat transfer coefficient, h , is given by:

$$h = \frac{\rho_g j_g c_p}{8\alpha} f_1 \quad (18)$$

where the friction factor f_1 is given by Equation (11). Note that for steam and common gases, the assumption of Prandtl number being unity is reasonable. We therefore obtain the following expression for $(\dot{q})_1$:

$$(\dot{q})_1 = \frac{1}{2} \frac{\rho_g j_g c_p (T_L - T_g)}{\alpha D} \quad (19)$$

where T_L is the temperature of the liquid phase (melt or melt simulant).

For a single sphere in uniform flow of a gas (Prandtl number = 1), the heat transfer coefficient is given by [9]

$$\frac{hd}{k_g} = 0.37 Re^{0.6}, \quad 25 \leq Re \leq 100 \times 10^3 \quad (20)$$

where Re is the Reynolds number for flow around the sphere and k_g is the thermal conductivity of the gas. Preliminary calculations show that for flow around droplets, we expect $100 \leq Re \leq 1000$. In this domain, the drag coefficient, C_D , for a sphere can be approximated as:

$$C_D = 7 Re^{-0.4}, \quad 100 \leq Re \leq 1000$$

Using this relation, and the assumption that Prandtl number is unity, Equation (20) gives:

$$h = 0.053 C_D \rho_g c_p (u_g - u_L) \quad (21)$$

If n is the number of droplets per unit volume of the duct, the net convective droplet to gas heat transfer rate is:

$$(\dot{q})_2 = n h = d^2 (T_L - T_g) \quad (22)$$

The droplet-gas interfacial drag is given by:

$$(F_{gL}^i)_2 = n C_D \frac{1}{2} \rho_g (u_g - u_L)^2 \frac{\pi d^2}{4} \quad (23)$$

Combining Equations (15), and (21)-(23), we get:

$$(\dot{q})_2 = 0.423 C_D f_L \frac{x}{D} \frac{u_L \rho_g^3 j^4 (1 - u_L/u_g)^3 c_p (T_L - T_g)}{\alpha \sigma^2 \rho_L (u_L/u_g)} \quad (24)$$

Thus, the total volumetric liquid-gas heat transfer rate is given by

$$\dot{q} = (\dot{q})_1 + (\dot{q})_2 \quad (25)$$

Note that in the above formulation we have neglected the radiative energy exchange between the gas and liquid.

2.5 Derivation of the Scaling Parameters

We are now in a position to derive the various dimensionless numbers that must have identical values for the full-scale reactor accident condition and the small-scale experiment for a "perfect" simulation. The procedure is to select fixed reference values for various variables, and then use these to rewrite the various conservation equations and boundary conditions in terms of dimensionless variables. The constant coefficients appearing in these equations are then the scaling parameters.

Let P_0 and T_0 be the pressure and temperature of steam in the reactor pressure vessel at the instant of vessel failure. If A_t is the area of cross section of the hole in the vessel bottom when steam blowdown starts, then, assuming steam to be a perfect gas, the instantaneous mass flow rate of gas, \dot{m}_g , (steam in reactor case) is given by:

$$\dot{m}_g = A_t f(\gamma) \frac{P_0}{\sqrt{RT_0}} \left\{ 1 - A_t f(\gamma) \frac{P_0}{\sqrt{RT_0}} \frac{1}{\rho_0 V_0} \frac{(1-\gamma)}{2} \tau \right\}^{\frac{1+\gamma}{1-\gamma}} \quad (26)$$

where V_0 is the volume of steam in the primary system, ρ_0 is the gas density in the pressure vessel at the instant of vessel failure, and $f(\gamma)$ is given by:

$$f(\gamma) = \gamma^{0.5} \left(\frac{2}{\gamma+1} \right)^{\frac{\gamma+1}{2(\gamma-1)}} \quad (27)$$

Equation (26) assumes that the flow is choked at the vessel orifice and therefore is valid only until the pressure in the primary system is greater than approximately twice the pressure in the cavity. Since no debris dispersal is expected to occur at the very low primary system pressures when this condition is reached, this restriction on Equation (26) is not of any practical consequence. We now define the reference values for various variables. These are given in Table 1, where P_∞ is the containment pressure, A_R is the area of cross section of the duct (cavity) at a specified location, and u_R is the velocity of gas at time $t = 0$ at this location if the gas pressure and temperature were P_∞ and T_0 , respectively. We can now define new dimensionless variables (denoted by the superscript $*$) as:

$$\begin{aligned} P^* &= P/P_\infty, & T_g^* &= T_g/T_L, & \rho_g^* &= \rho_g/\rho_R \\ j_g^* &= j_g/u_R, & j_L^* &= j_L/u_R, & c^* &= c/c_R \\ A^* &= A/L^2, & x^* &= x/L, & t^* &= t/t_R, \quad \frac{\partial}{\partial t} = \frac{1}{t_R} \frac{\partial}{\partial t^*} \\ \frac{\partial}{\partial x} &= \frac{1}{L} \frac{\partial}{\partial x^*}, & v_o^* &= v_o/L^3, & g_x^* &= g_x/g \end{aligned}$$

Because of the rather large heat capacity of the melt relative to the driving gas, the melt temperature is not expected to change significantly during its travel through the cavity. Thus the melt temperature T_L is treated as a constant in the present analysis.

We can now rewrite the conservation equations in terms of the dimensionless variables. The continuity equation for the gas phase, Equation (9) becomes:

$$\begin{aligned} \frac{\partial P^*}{\partial t^*} + \frac{j_g^*}{a} \frac{\partial P^*}{\partial x^*} - \left\{ f_1 \cdot \frac{\rho_R c_R^2}{P_\infty} \right\} \frac{c^{*2} \rho_g^* j_g^* (1-T_g^*)}{2a^2 T_g^* D^*} \\ - \left\{ C_D f_1 \cdot \frac{\rho_R c_R^2}{P_\infty} \cdot \frac{\rho_R^2 u_R^2}{\sigma \rho_L} \cdot \frac{u_L u_R}{\sigma} \right\} 0.423 c^{*2} \frac{x^*}{D^*} \frac{\rho_g^{*3} j_g^{*4} (1-u_L^*/u_g^*)^3 (1-T_g^*)}{a^5 T_g^* (u_L^*/u_g^*)} \end{aligned}$$

Table 1

Reference Values for Various Variables

Variable	Reference Value
Pressure	r_{∞}
Temperature	T_L
Density	$\rho_R = P_{\infty} / (RT_0)$
Velocity	$u_R = f(\gamma) \frac{A_t}{A_R} \frac{P_0}{\rho_R \sqrt{RT_0}}$
Sonic Speed	$c_R = \sqrt{\gamma RT_0}$
Length	L
Time	$t_R = L/u_R$

$$\begin{aligned}
& + \left\{ \frac{1}{\gamma} \cdot \frac{\rho_R c_R^2}{P_\infty} \right\} \frac{\rho_g^* c^*}{\alpha} \frac{\partial \alpha}{\partial t^*} + \left\{ \frac{\rho_R c_R^2}{P_\infty} \cdot \frac{L g}{c p T_L} \right\} \frac{\rho_g^* j_g^* c^*}{\alpha T_g^*} \frac{\partial j_g^*}{\partial x^*} \\
& - \left\{ \frac{\rho_R c_R^2}{P_\infty} \cdot \frac{u_R^2}{c p T_L} \right\} \frac{2 c^* \alpha^{*2} \cdot 3^*}{T_g^* \alpha^4 L^*} + \left\{ \frac{\rho_R c_R^2}{P_\infty} \right\} \frac{\rho_g^* c^*}{\alpha} \frac{\partial j_g^*}{\partial x^*} \\
& - \left\{ C_D f_1 \cdot \frac{\rho_R c_R^2}{P_\infty} \cdot \frac{\rho_R^2 u_R^2}{\sigma \rho_L} \cdot \frac{u_R^2}{c p T_L} \cdot \frac{u_R u_L}{\sigma} \right\} \frac{c^* \rho_g^* j_g^* (1 - u_L^*/u_g^*)^4}{T_g^* \alpha^7 (u_L^*/u_g^*)} \frac{x^*}{D^*} \\
& + \left\{ \frac{\rho_R c_R^2}{P_\infty} \right\} \frac{\rho_g^* j_g^* c^*}{\alpha A^*} \frac{dA^*}{dx^*} = 0
\end{aligned} \tag{28}$$

The liquid continuity equation becomes:

$$\frac{\partial}{\partial t^*} (1 - \alpha) + \frac{\partial j_L^*}{\partial x^*} + \frac{j_L^*}{A^*} \frac{dA^*}{dx^*} = 0 \tag{29}$$

The momentum equation for the gas phase, Equation (3) becomes:

$$\begin{aligned}
\rho_g^* \frac{\partial j_g^*}{\partial t^*} - \frac{\rho_g^* j_g^*}{\alpha} \frac{\partial \alpha}{\partial t^*} + \rho_g^* j_g^* \frac{\partial}{\partial x^*} \left(\frac{j_g^*}{\alpha} \right) + [f_1] \frac{2 \rho_g^* j_g^*}{D^* \alpha^2} \\
+ \left\{ C_D f_1 \cdot \frac{\rho_R^2 u_R^2}{\sigma \rho_L} \cdot \frac{u_L u_R}{\sigma} \right\} \frac{\rho_g^* j_g^* (1 - u_L^*/u_g^*)^4}{\alpha^5 (u_L^*/u_g^*)} \frac{x^*}{D^*} \\
- \left\{ \frac{g_L}{u_R} \right\} \alpha \rho_g^* g_x^* + \left\{ \frac{P_\infty}{\rho_R u_R} \right\} \alpha \frac{\partial P^*}{\partial x^*} = 0
\end{aligned} \tag{30}$$

The momentum equation for the liquid phase, Equation (4) becomes:

$$\begin{aligned} \frac{\partial j_L^*}{\partial t^*} - \frac{j_L^*}{(1-\alpha)} \frac{\partial(1-\alpha)}{\partial t^*} + j_L^* \frac{\partial}{\partial x^*} \left[\frac{j_L^*}{(1-\alpha)} + \left\{ \frac{P_\infty}{\rho_L u_R^2} \right\} (1-\alpha) \frac{\partial P^*}{\partial x^*} - \left\{ \frac{gL}{u_R^2} \right\} (1-\alpha) g_x^* \right. \\ \left. - \left\{ f_i \cdot \frac{\rho_R}{\rho_L} \right\} \frac{2 \rho_g^* j_g^{*2}}{D^{*2}} + \left\{ \frac{\mu_L}{L \rho_L u_R} \right\} \frac{8 j_L^*}{D^* (1-\alpha) m^*} \right. \\ \left. - \left\{ C_D f_i \cdot \frac{\rho_R^2 u_R^2}{\sigma \rho_L} \cdot \frac{u_R \mu_L}{\sigma} \cdot \frac{\rho_R}{\rho_L} \right\} \frac{\rho_g^* j_g^{*5} (1-u_L^*/u_g^*)^4}{a^5 (u_L^*/u_g^*)} \frac{x^*}{D^*} \right] = 0 \end{aligned} \quad (31)$$

The energy equation for the gas phase, Equation (6) becomes:

$$\begin{aligned} \frac{\partial T_g^*}{\partial t^*} + \frac{j_g^*}{\alpha} \frac{\partial T_g^*}{\partial x^*} - \left\{ \frac{P_\infty}{\rho_R c_p T_L} \right\} \left[\frac{1}{\rho_g^*} \frac{\partial P^*}{\partial t^*} + \frac{j_g^*}{\rho_g^* \alpha} \frac{\partial P^*}{\partial x^*} \right] - \left(\frac{\gamma-1}{\gamma} \right) \frac{T_g^*}{\alpha} \frac{\partial \alpha}{\partial t^*} + \left\{ \frac{gL}{c_p T_L} \right\} \frac{g_x^* j_g^*}{\alpha} \\ - \left\{ \frac{f_i u_R^2}{c_p T_L} \right\} \frac{2 j_g^{*3}}{a^4 D^*} - \left\{ C_D f_i \cdot \frac{\rho_R^2 u_R^2}{\sigma \rho_L} \cdot \frac{u_R^2}{c_p T_L} \cdot \frac{\mu_L u_R}{\sigma} \right\} \frac{\rho_g^* j_g^{*6} (1-u_L^*/u_g^*)^4}{a^7 (u_L^*/u_g^*)} \frac{x^*}{D^*} \\ = \left\{ f_i \right\} \frac{j_g^* (1-T_g^*)}{2 a^2 D^*} + \left\{ C_D \cdot f_i \cdot \frac{\rho_R^2 u_R^2}{\sigma \rho_L} \cdot \frac{\mu_L u_R}{\sigma} \right\} \frac{0.423 \rho_g^* j_g^{*4} (1-T_g^*) (1-u_L^*/u_g^*)^3}{a^5 (u_L^*/u_g^*)} \frac{x^*}{D^*} \end{aligned} \quad (32)$$

The boundary and initial conditions for the above set of conservation equations are:

At $t^* = 0$:

$$\begin{aligned} P^* = 1, \quad j_g^* = 0, \quad j_L^* = 0, \\ \alpha = 1; \quad \text{at } x = 0 \\ \alpha = 1 - 4m^*/D^*; \quad \text{for } x > 0 \end{aligned} \quad (33)$$

At $x^* = 0$:

$$a = 1, \quad j_L^* = 0$$

From Equation (26) and the definition for u_g , we have the boundary condition for the gas mass flux at $x^* = 0$ as:

$$\rho_g^* A^* j_g^* = A_R^* \left[1 - \frac{A_P^* (1-\gamma) t^*}{2} \cdot \left\{ \frac{P_\infty}{P_0 V_0^*} \right\} \right]^{\frac{1+\gamma}{1-\gamma}} \quad (34)$$

Let P_1 be the pressure at $x^* = 0$ at any time t , then, assuming isentropic expansion of gas from the reactor pressure vessel, the gas temperature at $x^* = 0$ is given by:

$$T_g = T_0 (P_1/P_0)^{\frac{\gamma-1}{\gamma}}$$

or

$$T_g^* = (P_1^*)^{\frac{\gamma-1}{\gamma}} \left\{ \frac{T_0}{T_L} \left(\frac{P_\infty}{P_0} \right)^{\frac{\gamma-1}{\gamma}} \right\} \quad (35)$$

If the length of the cavity equals bL , then, $P^* = 1$ at $x^* = b$.

We are now in a position to derive the similarity parameters for the debris dispersal problem. It is clear that if all the parameters within curly brackets in Equations (28) through (32) and the above boundary conditions are the same for the full-scale reactor cavity (prototype) and the model experiment, we have an identical set of equations and boundary conditions for the model and the prototype. Therefore, these parameters are the scaling parameters. Before we list these parameters, let us consider two other parameters that are implicit in the conservation equations. The requirement that A^* (function of x^*), appearing in conservation equations, be the same for the model and the prototype, implies complete geometrical similarity of the cavity model to the full-scale reactor cavity. The requirement that the dimensionless film thickness, m^* be the same between the experiment and the full-scale accident implies that the amount of melt simulant used in the experiment should be scaled volumetrically.

A careful look at the various dimensionless parameters (quantities within the curly brackets in Equations (28) through (35)) shows that not all of these

are independent. In fact, many of the parameters can be expressed as the product of some of the other groups. The parameters have been carefully examined and 10 independent† dimensionless groups have been obtained:

$$\left. \begin{aligned}
 \Pi_1 &= C_D \cdot \frac{\rho_R^2 u_{RL}^2}{\sigma \rho_L} \cdot \frac{u_L u_R}{\sigma}, \quad \Pi_2 = \frac{u_R^2}{c_{PTL}}, \quad \Pi_3 = f_1, \\
 \Pi_4 &= \frac{gL}{u_R^2}, \quad \Pi_5 = \frac{\rho_R c_R^2}{P_\infty}, \quad \Pi_6 = \frac{\rho_R}{\rho_L}, \quad \Pi_7 = \frac{P_\infty}{\rho_R u_R^2}, \\
 \Pi_8 &= \frac{u_L}{\rho_L u_{RL}}, \quad \Pi_9 = \frac{P_0 V_0^*}{P_\infty}, \quad \Pi_{10} = \frac{T_0}{T_L} \left(\frac{P_\infty}{P_0} \right)^{\frac{\gamma-1}{\gamma}}
 \end{aligned} \right\} \quad (36)$$

It is emphasized that there is nothing unique about the particular set of scaling parameters given above. One can form an alternative set of 10 independent dimensionless parameters by recombining the individual parameters in Equation (36). The only requirement for achieving complete similarity between the model experiments and the full-scale case is that all the 10 dimensionless numbers for the experiment be identical to those for the full-scale case. We shall now use Equation (36) to derive an alternate set of dimensionless groups. The object of the exercise is to have groups that are either well-known or have a clear physical meaning.

Using the definition of u_R , we have

$$\Pi_8 = \frac{P_\infty}{\rho_R u_R^2} = \left(\frac{P_\infty}{P_0} \right)^2 \frac{A_R^2}{A_t^2} \frac{1}{[f(\gamma)]^2}$$

From Equation (11)

$$f_1 = f_s \left[1 + \frac{360 m^*}{D^*} \right]$$

Thus f_1 in Equation (36) can be replaced†† by the single phase smooth pipe friction factor f_s since both m^* and D^* are matched between the model and the full-scale case. However, the friction factor f_s is only dependent upon the duct Reynolds number, i.e.,

†Note that $\gamma = \rho_R c_R^2 / P_\infty$.

††Because m^*/D^* is the same for the model and the prototype.

$$f_s = f\left(\frac{\rho_g j_g^D}{u_g a}\right) = f\left(\frac{\rho_R u_R L}{u_g} \cdot \frac{\rho_g j_g^{D*}}{a}\right) \quad (37)$$

Since the dimensionless variables in the second group are the same between the model and the prototype, the requirement that f_s be matched can be replaced by the requirement that $\rho_R u_R L / u_g$ be the same between experiment and full scale.

The drag coefficient C_D experienced by a melt droplet should only be a function of the droplet Reynolds number. Since the droplet diameter is given by Equation (13), we have:

$$C_D = f\left(\frac{12\sigma}{u_g u_g (1-u_L/u_g)}\right) = f\left(\frac{\sigma}{u_R u_g} \cdot \frac{12}{u_g (1-u_L^*/u_g^*)}\right) \quad (38)$$

Therefore, the requirement that C_D be the same between the model and the full scale is identical to the requirement that the group $\sigma/(u_R u_g)$ be the same.

By making use of the above considerations, it is now easy to show that the group of dimensionless variables represented by Equation (36) can be replaced by the first 10 (N_1 through N_{10}) independent dimensionless numbers given in Table 2. Thus, the requirements for achieving complete similarity between the model experiments and the full-scale reactor cavity are that all these scaling parameters be matched between the model and the prototype. In addition, the other requirements are: (i) complete geometrical similarity, (ii) the Prandtl number of the gas phase to be approximately unity (implicit in our modeling of liquid-gas heat transfer), and (iii) that the amount of melt-simulant used in the experiments be scaled according to the volume of the cavity model (i.e., melt volume $\sim L^3$).

We also note that the fraction of debris dispersed, F_d (dimensionless extent of melt dispersal), can be expressed as a function of all the dimensionless parameters, i.e.,

$$F_d = f(N_1, N_2, N_3, N_4, \dots)$$

Therefore, if all the dimensionless parameters could be matched between the full-scale case and our model experiments, then the experimental results could be directly applied to the full-scale case. However, because of the rather large number of dimensionless numbers specified in Table 2, it is extremely unlikely that one would be able to match all these between the small-scale experiments and the full scale. Therefore, it is necessary to look at the physical meaning of various dimensionless numbers so that one may assess the effect of individual parameter on debris dispersal.

Table 2. Similarity Parameters for the Debris Dispersal Process

(a) Dimensionless Numbers*:

$$N_1 = \frac{\sigma \rho_L}{\rho_R^2 u_{R,L}^2}, \quad N_2 = \frac{\rho_R}{\rho_L} \cdot \left(\frac{\rho_R^2 u_{R,L}^2}{\sigma \rho_L} \right), \quad N_3 = \frac{\sigma}{u_g u_R},$$

$$N_4 = \frac{P_o V_o^*}{P_\infty}, \quad N_5 = \frac{\rho_R u_R^2}{\sqrt{\rho_L g \sigma}}, \quad N_6 = \frac{u_L u_R}{\sigma} \sqrt{\frac{\rho_R}{\rho_L}} \frac{1}{N_\mu^{0.8}},$$

$$N_7 = \left(\frac{P_o}{P_\infty} \right)^2 \frac{A_c^2}{A_R^2}, \quad N_8 = M_\infty = u_R / c_R,$$

$$N_9 = \frac{T_o}{T_L} \left(\frac{P_\infty}{P_o} \right)^{\frac{\gamma-1}{\gamma}}, \quad N_{10} = u_R^2 / (c_p T_L)$$

$$N_{11} = \frac{\text{Volume of Melt Simulant}}{L^3}, \quad \text{Prandtl number of gas phase} = 1$$

where:

$$N_\mu = \frac{u_L}{\left[\rho_L \sigma \sqrt{\frac{\sigma}{\rho_L g}} \right]^{0.5}}$$

(b) Other Similarity Requirements:

Cavity model be geometrically similar to the full-scale reactor cavity.

*The subscript R refers to the reference values given in Table 1.

It is easy to show that $N_7 = (\gamma/[f(\gamma)]^2) N_8^2$. Thus either N_7 or N_8 could be replaced by γ .

2.6 Physical Interpretation of Dimensionless Parameters

Consider a melt droplet of diameter d , initially at rest in a gas flow field of uniform velocity u_R . If the drag coefficient for the droplet is assumed to be a constant, it is easy to show that the time constant of the droplet, τ_d (time at which the particle velocity equals $0.63 u_R$) is proportional to:

$$\tau_d = \frac{\rho_L d}{\rho_R u_R}$$

However, the particle diameter is given by the condition that critical Weber number equals 12, i.e.,

$$d = \frac{12\sigma}{\rho_R u_R^2} \quad (39)$$

Therefore,

$$\tau_d = \frac{\rho_L \sigma}{\rho_R^2 u_R^3}$$

Now, the fluid transit time through the cavity τ_f is proportional to

$$\tau_f = L/u_R$$

Therefore

$$\frac{\tau_d}{\tau_f} = \frac{\sigma \rho_L}{\rho_R^2 u_R^2 L} = N_1$$

Thus the first dimensionless number, N_1 is proportional to the ratio of droplet time constant to the fluid transit time through the cavity. Obviously, the smaller this number, larger would be the tendency of droplets to follow the fluid stream lines, and therefore larger the expected debris dispersal.

The number N_2 is simply the density ratio ρ_R/ρ_L divided by the group N_1 . Since we can expect debris dispersal to increase when the density ratio ρ_R/ρ_L is increased, it follows (from our previous discussion of N_1) that as the value of N_2 is increased, the fraction of debris dispersed should also increase.

Let us consider a melt droplet of diameter d (given by Equation (39)) at rest. Then, the droplet Reynolds number is given by:

$$\text{Droplet Reynolds Number} = \frac{\rho_R u_R d}{\mu_g} = \frac{12\sigma}{\mu_g u_R} = N_3$$

Therefore, the dimensionless group N_3 can be interpreted as a number proportional to the droplet Reynolds number. Since the drag coefficient decreases as the Reynolds number is increased, it follows that the debris dispersal decreases as N_3 is increased.

The number N_4 , which appears as a result of satisfying the gas mass flux boundary condition at $x = 0$, can be thought of as the dimensionless gas blow-down time. In fact, it is not difficult to show that

$$(\text{pressure vessel blowdown time}) \frac{u_R}{L} = \text{constant} \cdot N_4 \cdot (\text{very weak function of } P_0/P_\infty)$$

$$= N_4$$

So, obviously as N_4 is increased the debris dispersal can only increase.

N_5 is the square of the well-known Kutateladze number. For a two-phase annular flow in a pipe, flow reversal (liquid film changing its direction of motion from downward direction to the same direction as the upward flowing gas) is predicted to occur [7] when N_5 exceeds 10. As shown below, the Kutateladze number can also be interpreted as the ratio of drag force on the particle (liquid droplet) trying to sweep it out of the cavity to the gravitational force trying to keep it within the cavity.

$$\left[\frac{\text{Drag}}{\text{Gravitational Force}} \right]^{0.5} \sim \left[\frac{\rho_R u_R^2 d^2}{\rho_L d^3 g} \right]^{0.5} \sim \left[\frac{\rho_R u_R^2}{\rho_L g} \right]^{0.5} = N_5$$

Therefore, we can only expect the debris dispersal to increase with increasing N_5 .

N_6 is the only group which is dependent upon the liquid phase viscosity. Its form was suggested by the work of Ishii and Grolmes [10], who show that the inception criteria for droplet entrainment during a two-phase concurrent film flow is: $N_6 > 1$. If N_6 is less than unity, no droplet entrainment could be expected. On the other hand, the larger the value of N_6 above unity, the larger the expected droplet entrainment rate, and hence the larger the expected debris dispersal.

As shown earlier on page 23, the group N_7 is proportional to the term $\rho_R u_R^2 / P_\infty$, and this term occurs in the gas momentum equation (where it is negligible compared to the interfacial drag term) and the gas energy equation. Although it is difficult to judge the importance of this term, it is clear that

debris dispersal can only increase with increasing N_7 . This is because intuitively it is obvious that if P_0 (primary system pressure) or A_t (hole size in the vessel bottom) were increased, we would have larger gas velocities in the cavity, and therefore larger debris dispersal from the cavity.

The group N_8 is simply the Mach number and the nature of its effect on debris dispersal is not obvious. The number N_9 , which appears as a result of satisfying the gas temperature boundary condition at the beginning of the cavity ($x^* = 0$), is proportional to the dimensionless gas temperature at $x^* = 0$. The larger this number, the less the temperature difference between the gas and the melt, and hence the smaller the increase in gas velocities due to heat transfer, and therefore less debris dispersal.

The group N_{10} appears as a coefficient in two of the terms in the gas energy equation. It appears in a term which represents the work done on the gas due to liquid drag ($F_{GLjg}/(\rho_g a^2)$). This term is smaller than the gas-liquid heat transfer rate, and as N_{10} is increased, this term tends to increase the gas temperature and hence increase the debris dispersal. The second term in which N_{10} appears as a coefficient involves the pressure gradient. This term is also smaller than the liquid-gas heat transfer rate, and its effect on debris dispersal is in an opposite direction to that of the first term. Therefore, this term may not be very important. It appears that increasing N_{10} may result in a small increase in the debris dispersal.

3. EXPERIMENTAL SIMULATION OF MELT DISPERSAL FROM REACTOR CAVITIES

3.1 Selection of Plant-Specific Reactor Cavities

The Industry Degraded Core Rulemaking Program (IDCOR) has classified PWR reactor cavities according to geometry into 14 types. IDCOR's position on the expected debris dispersal from these cavity types during a high-pressure melt ejection accident is given in the IDCOR Technical Report 85.2 [11]. Based upon these views, the 14 cavity types can be further classified on the basis of expected debris dispersal into 4 groups. These are shown in Table 3. The table also shows the number of reactor units of each type owned by the IDCOR participant utilities. The cavity Type A through I is the IDCOR classification based upon the geometry.

As a first step towards resolving the debris dispersal issue, we have chosen to study debris dispersal from one cavity type from each of the Groups 1, 3, and 4. No cavity type from Group 2 was selected because this group has only two reactor units out of a total of 72 units. We have selected the Zion from Group 1, the Watts Bar (similar to Sequoyah) from Group 3, and the Surry from Group 4.

3.2 Selection of Accident Initial Conditions

Before we can select the experimental parameters for our simulant debris dispersal tests, we must first select the full-scale reactor conditions that we want to simulate. In other words, one must first decide upon the set of initial conditions (P_0 , T_0 , mass of melt, etc.) at the instant of high-pressure melt ejection in the full-scale reactor. We realize at the outset that the set of initial conditions is not unique; that is, given a high-pressure melt ejection accident, there are many possible sets of initial conditions. The reason is as follows. There are many accident sequences (each sequence having a certain probability of occurrence) that can lead to a high-pressure melt ejection accident. Since the sequences are different, each may lead to a potentially different initial condition. In addition, since the operator action, which is not completely predictable, is an integral part of each sequence, even a given sequence may lead to many sets of initial conditions. Therefore, in reality we have a large range of initial conditions with associated probabilities. The detailed (and accurate) information about this range of possible initial conditions is however, not currently available. It should in principle, be provided by other NRC programs (SASA, MELPROG). We note here that, the purpose of our current experiments is merely to characterize the debris dispersive nature of various cavity designs. The experiments are not intended to simulate the entire range of possible initial conditions.

In the absence of the above-mentioned detailed information about the initial conditions, we have selected a set of base case initial conditions based upon what is currently believed [12,13,14] to be the range of various initial parameters. In addition, to show the sensitivity of various dimensionless groups (discussed in Chapter 2) to the assumed initial conditions, we have selected two additional sets of initial conditions for each of the cavity types. These initial conditions, which are primarily based upon NRC Standard Problem Numbers 1 and 2 [14], are given in Table 4.

Table 3. Summary of IDCOR Reactor Cavity Configurations

Group 1	Group 2	Group 3	Group 4
Large Debris Dispersal	Medium Debris Dispersal	Small Debris Dispersal	None/Little Debris Dispersal
A (6, Zion, etc.) B (5, Indian Point, etc.) F(5, Calvert Cliffs, etc.) J(2, San Onofre 2&3) N(1, Yankee Rowe)	L(2, Bellefonte 1&2)	C(12, Sequoyah, etc.) K(2, WNP1, etc.) M(5, Calloway, etc.)	D(10, Surry, etc.) E(2, South Texas 1&2) G(3, Oconee 1,2,3) H(12, Summer 1, etc.) I(5, St. Lucie 1, etc.)

NOTE: Cavities are grouped according to anticipated (by IDCOR) debris dispersal from reactor cavities during a high pressure melt ejection accident. The numerical number after the cavity type (IDCOR classification) indicates the number of reactor units quoted in the IDCOR Technical Report 85.2.

Table 4. Initial Conditions for the Full-Scale Reactor Cavities

Case	P ₀ (MPa)	P _∞ (MPa)	T _L (K)	T ₀ (K)	V ₀ (m ³)	hole* Diameter (m)	Mass of Core Melt (kg)
(a) Zion:							
ZR1 (Base Case)	7.0	0.4	2533.0	558.8	340.0	0.4	134 × 10 ³
ZR2	5.0	0.4	2533.0	536.0	340.0	0.55	134 × 10 ³
ZR3	15.0	0.4	2533.0	614.0	340.0	0.4	134 × 10 ³
(b) Surry:							
SR1 (Base Case)	7.0	0.193	2533.0	558.8	268.0	0.4	127 × 10 ³
SR2	5.0	0.193	2533.0	536.0	268.0	0.55	127 × 10 ³
SR3	15.0	0.193	2533.0	614.0	268.0	0.4	127 × 10 ³
(c) Watts Bar:							
WBR1 (Base Case)	7.0	0.14	2533.0	558.8	357.0	0.4	130 × 10 ³
WBR2	5.0	0.14	2533.0	536.0	357.0	0.55	130 × 10 ³
WBR3	15.0	0.14	2533.0	614.0	357.0	0.4	130 × 10 ³
*Diameter of the hole in the reactor pressure vessel bottom head at the beginning of the steam blowdown.							

The initial conditions are used to calculate the various dimensionless groups given in Table 2. The experimental parameters are then chosen so as to yield as close an agreement in the dimensionless numbers between the full-scale base case and the experiments as possible. By selecting the particular set of base initial conditions given in Table 4, we do not mean to imply that this is the most probable set or the set with the severest consequences. The data or analysis to make a rational choice based upon these arguments is lacking.

In Section 2.1 we discussed two limitations of our debris dispersal experiments. Let us now consider an additional impediment to performing a perfectly scaled simulant experiment. For the full-scale reactor, the melt temperature is much larger than the steam temperature. Therefore, due to

large melt-steam heat transfer, steam velocity within the cavity will be a strong function of position. Because of practical constraints, it is impossible for us to use very high melt simulant temperatures. As a result, we cannot simulate the variation of gas velocity within the cavity due to heat transfer effects. This difficulty is reflected in the fact that we cannot match the dimensionless group N_g between the full-scale accident condition and the simulant experiment. However, as long as we understand that, (i) it is the motion of gas that is responsible for debris dispersal and not the gas temperature, and (ii) that the purpose of our experiments is to characterize the dispersive nature of various cavity designs, we can instead try to scale our experiments to "modified" accident conditions which have already taken into account the rather large melt-steam heat transfer rates. In other words, we can simulate the fact that as a result of melt-steam heat transfer the average gas velocity in the cavity is going to increase. We do this as follows.

Since the heat capacity of steam flowing through the cavity is much smaller than that of the core-melt, and also because the surface area available for melt-steam heat transfer is likely to be large, we expect that steam would heat up to the melt temperature within a very short distance. Therefore, we assume that most of the melt-steam heat transfer occurs just below the reactor pressure vessel within the cavity. In other words, although at $x = 0$ within the cavity we still have the same mass flux of steam coming into the cavity, it is now assumed to be at a much higher temperature. Mathematically, this consists of replacing the conditions of steam in the primary system, T_0 , P_0 , V_0 , by the modified conditions T'_0 , P'_0 , and V'_0 . We assume that the modified steam temperature within the primary system, T'_0 equals the liquid temperature, T_L . We find P'_0 and V'_0 by satisfying the requirement that the computed steam mass flux into the cavity using the modified conditions (P'_0 , V'_0 , T'_0) be identical to the computed steam mass flux using the actual primary system conditions (P_0 , V_0 , T_0). The steam mass flux $\dot{m}_g(t)$ at any time t into the cavity is given by (see Eq. (26)):

$$\dot{m}_g(t) = \dot{m}_g^0 \left[1 - \frac{\dot{m}_g^0}{M_0} \frac{(1-\gamma)}{2} t \right]^{\frac{\gamma+1}{1-\gamma}} \quad (40)$$

where \dot{m}_g^0 is the steam mass flow rate into the cavity at $t = 0$, and M_0 is the total mass of steam in the primary system at $t = 0$. Therefore, if both \dot{m}_g^0 and M_0 are the same for the actual and "modified" conditions, we will have identical $\dot{m}_g(t)$. Since

$$\dot{m}_g^0 = A_t f(\gamma) \frac{P_0}{\sqrt{RT_0}} = A_t f(\gamma) \frac{P'_0}{\sqrt{RT'_0}}$$

and

$$M_0 = \rho_0 V_0 = \rho'_0 V'_0,$$

we have

$$P'_0 = P_0 \left(\frac{T_L}{T_0} \right)^{0.5}, \quad V'_0 = V_0 \left(\frac{T_L}{T_0} \right)^{0.5}, \quad T'_0 = T_L \quad (41)$$

We shall use the above values of P'_0 , T'_0 , and V'_0 to compute the dimensionless scaling parameters (given in Table 2) for the full-scale accident conditions.

3.3 Experimental Method and Parameters

The schematic of the experimental facility designed to carry out debris dispersal experiments using small-scale (1/42nd) transparent models of the reactor cavities is shown in Figure 3. The pressure vessels PV_1 and PV_2 , the melt holder MH, and the ball valve BV are all wrapped with heating tapes and insulation. Four temperature controllers are used to control temperatures at various locations. The cavity model C under test is held below the melt holder and is enclosed in a transparent plexiglas enclosure B. Since molten Wood's metal (melting point 345 K) is used as one of the melt simulants, hot air is circulated through the plexiglas enclosure to keep the cavity model at approximately 373 K to prevent freezing of the Wood's metal in the cavity. The melt holder (MH) and the ball valve (BV) are heated to about 460 K when Wood's metal is used as the melt simulant. A photograph of this facility is presented in Figure 4.

To begin an experiment, the cavity, the melt holder, and the pressure vessels are heated to appropriate temperatures. Then, a volumetrically scaled quantity of the melt simulant is placed in the melt holder and the ball valve is closed. When the melt simulant temperature reaches the desired value, the pressure vessels are charged with the simulant gas (nitrogen or helium) to the appropriate pressure. The experiment is initiated by opening the ball valve. This results in the rupture of an aluminum foil diaphragm (D), and thus a known mass of melt simulant is injected into the cavity model from an orifice above the cavity floor. This is followed immediately by the blowdown of gas from the pressure vessels. The debris that leaves the cavity (via exit E) is either trapped in the duct P or the collection tank. During the experiment, high-speed movies of the melt simulant-gas interaction in the cavity are taken and, at the end of the experiment, the mass of melt simulant trapped in the cavity is measured.

Figure 5 shows the photographs of the Zion, the Surry, and the Watts Bar cavity models. Schematics of these cavity models are shown in Figure 6(a-c). The experimental parameters for the various debris dispersal experiments performed using the 1/42nd-scale models of the Zion, the Surry, and the Watts Bar cavities are given in Table 5. The second column, which gives the case number for each run, is used to characterize the experimental parameters. In other words, all runs having the same case number have nominally the same set of parameters. The dimensionless parameters which characterize each experiment are presented in Chapter 4.

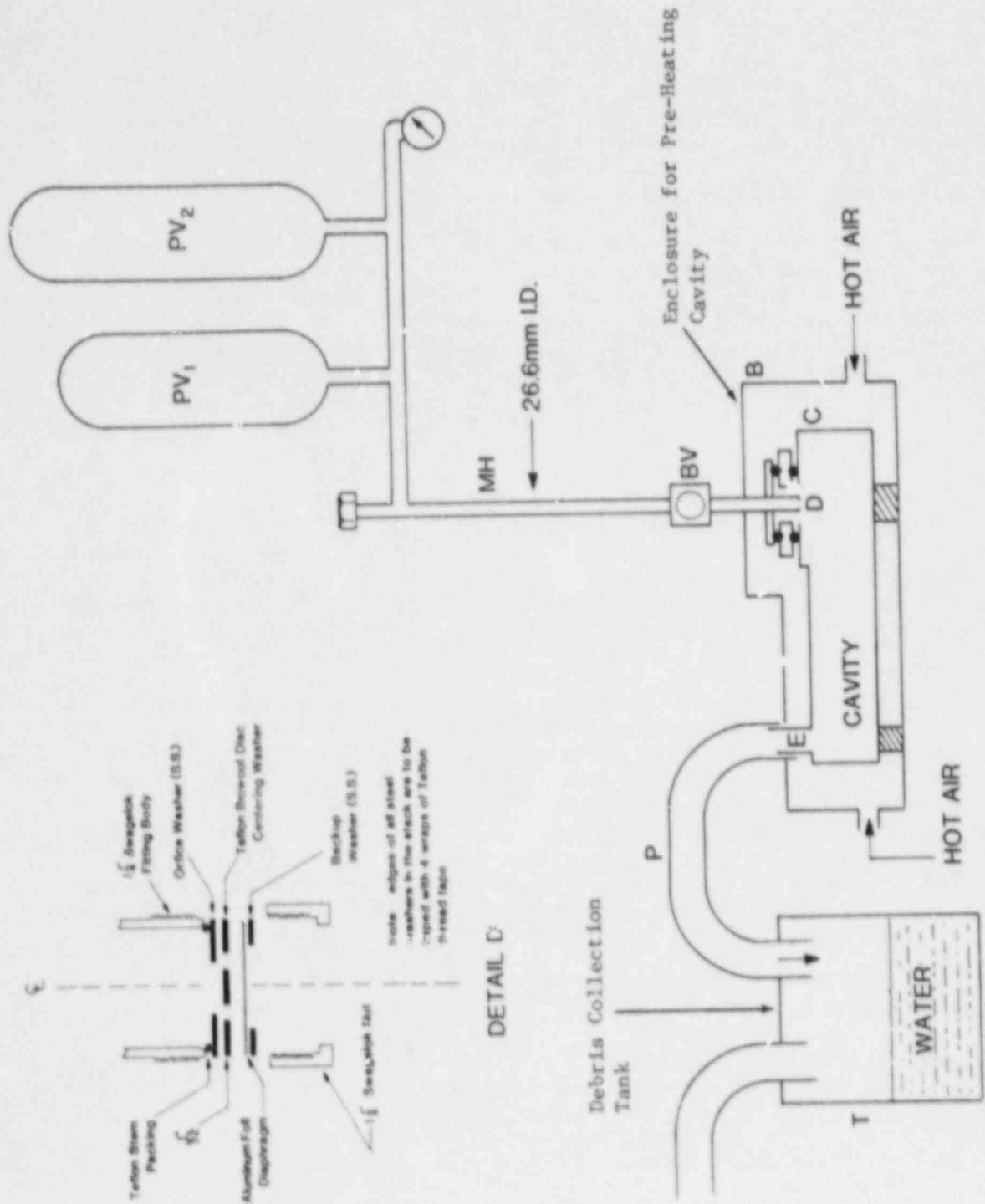


Figure 3 Schematic of Experimental Setup (melt holder MH, ball valve BV, and pressure vessels PV_1 , and PV_2 are all wrapped with heating tapes and insulated)

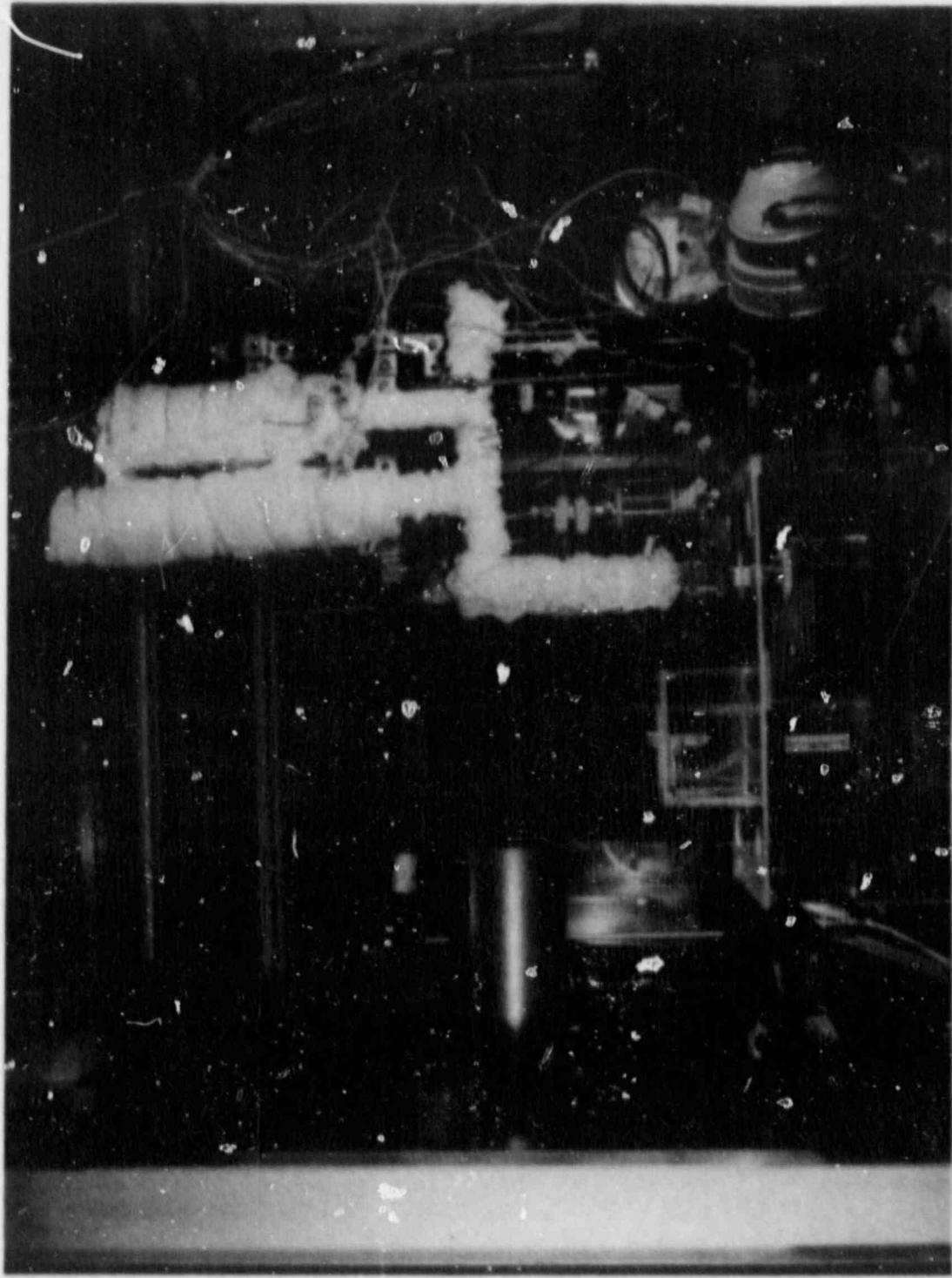


Figure 4 Photograph of the Experimental Facility Showing a Model of the
Watts Bar Cavity Under Test

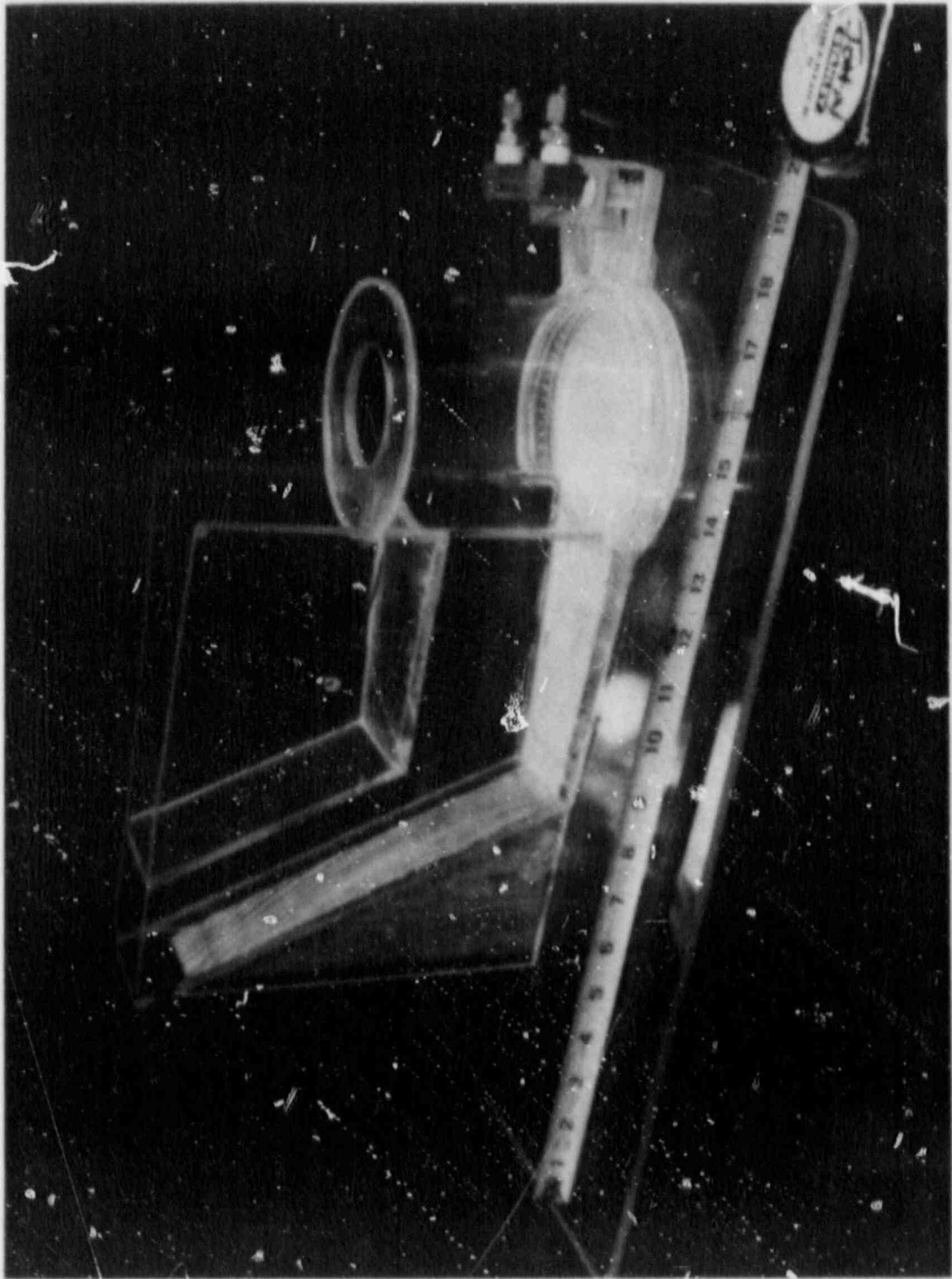


Figure 5(a) Photograph of the Zion Reactor Cavity Model

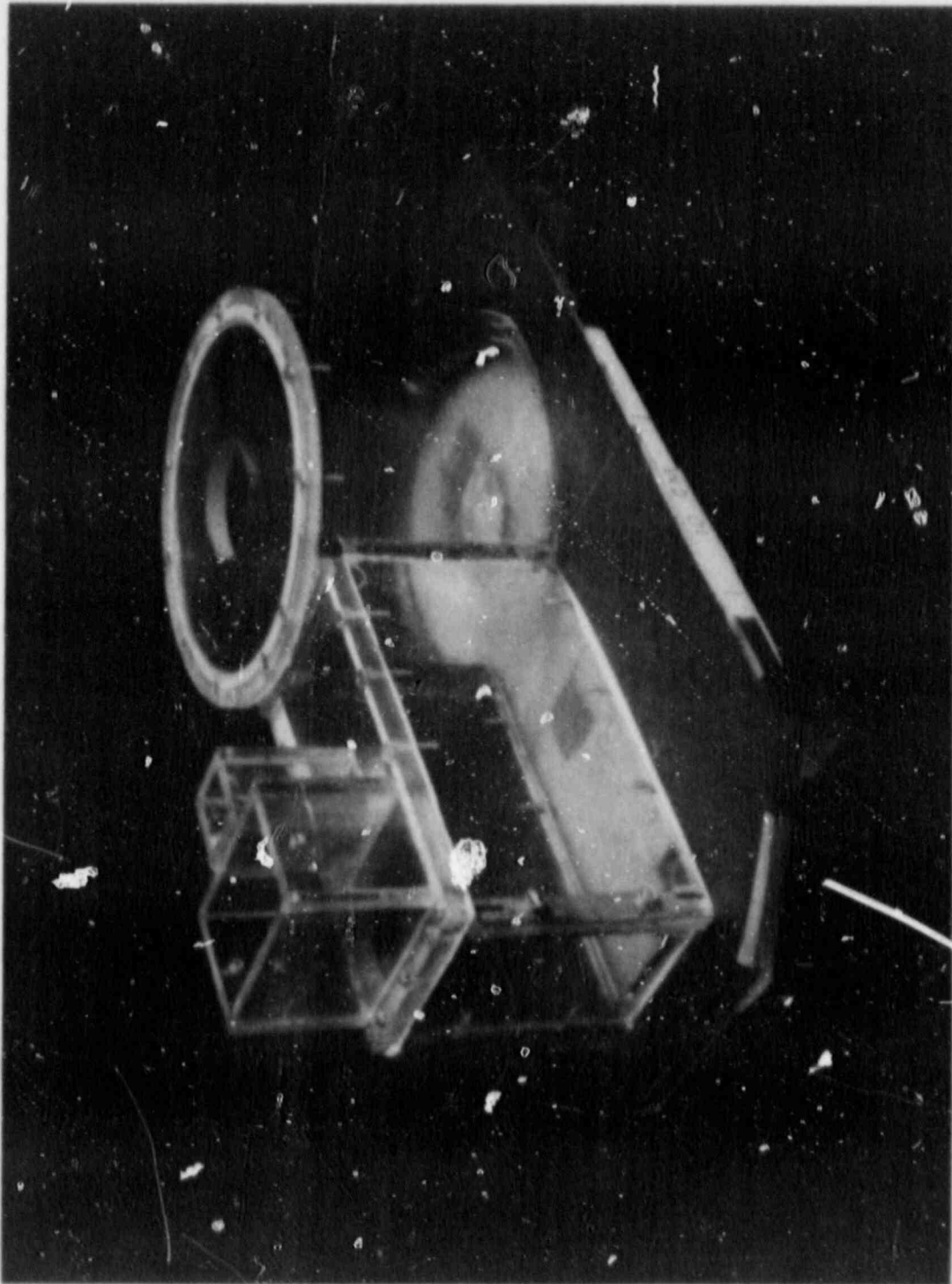


Figure 5(b) Photograph of the Surry Reactor Cavity Model

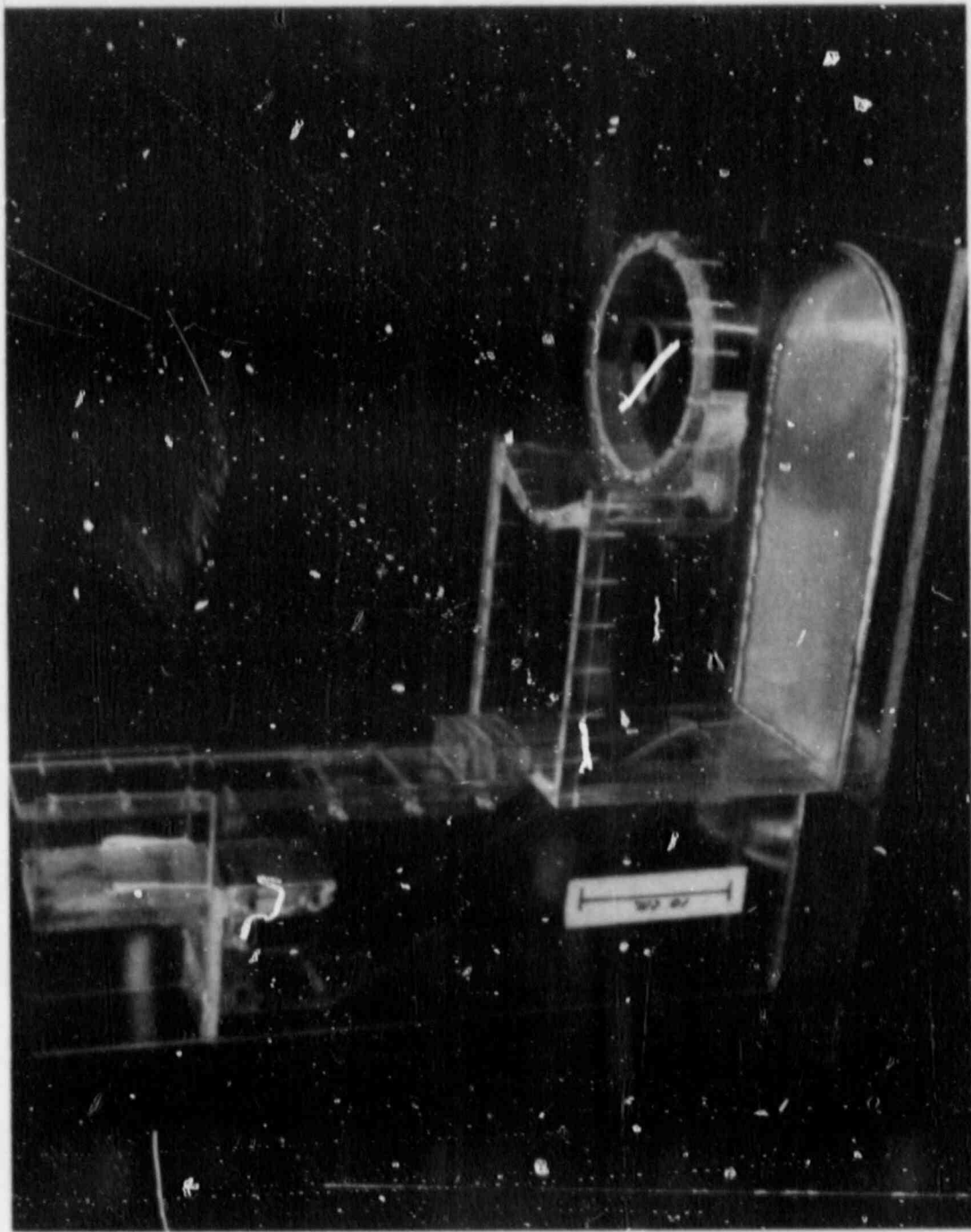


Figure 5(c) Photograph of the Watts Bar Reactor Cavity Model

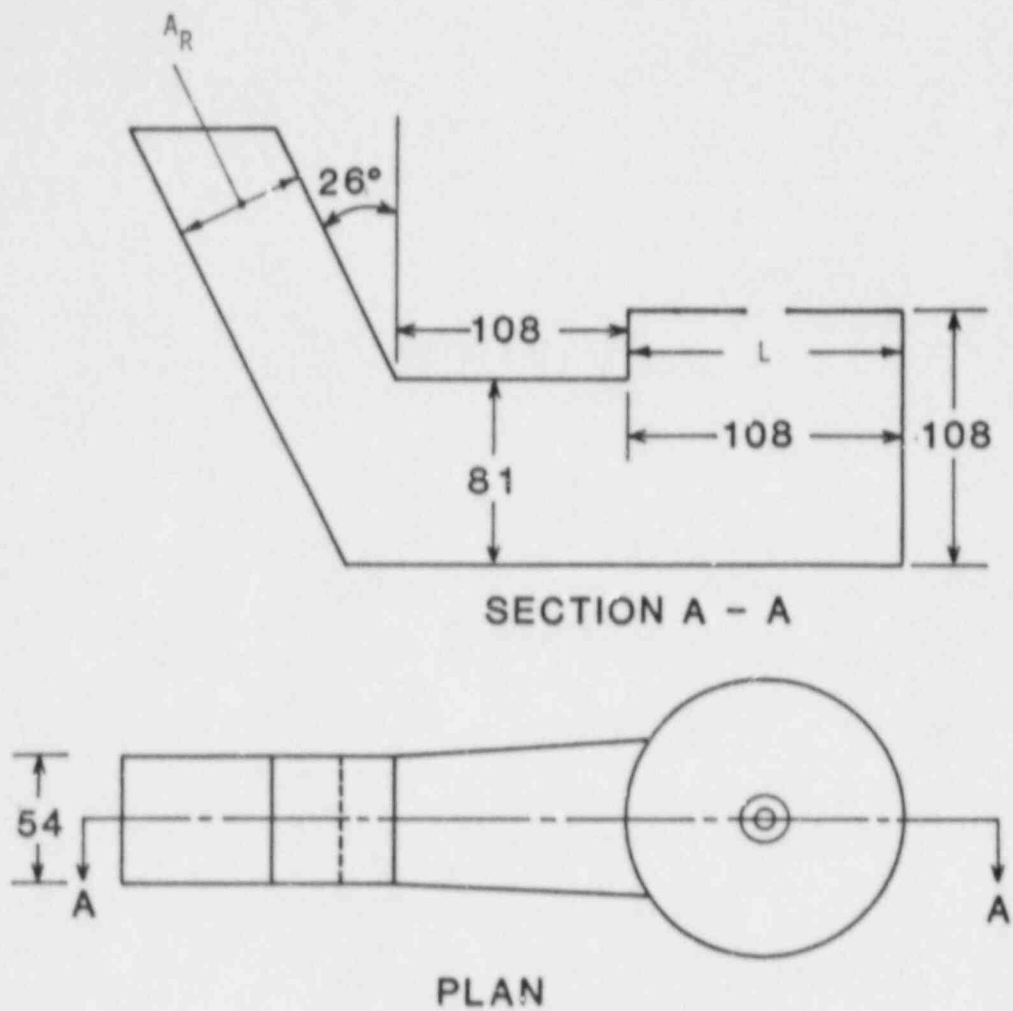


Figure 6(a) Schematic of the Zion Cavity Model. All dimensions are in mm. L and A_R are the reference values of the length scale and the cavity cross-sectional area, respectively.
 $A_R = 0.00291 \text{ m}^2$

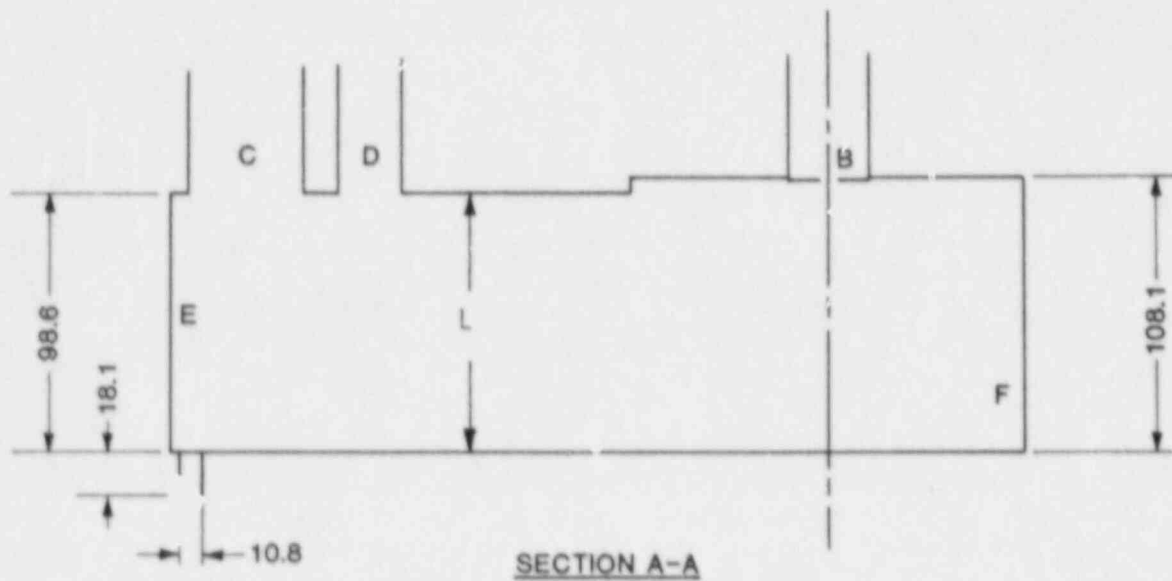
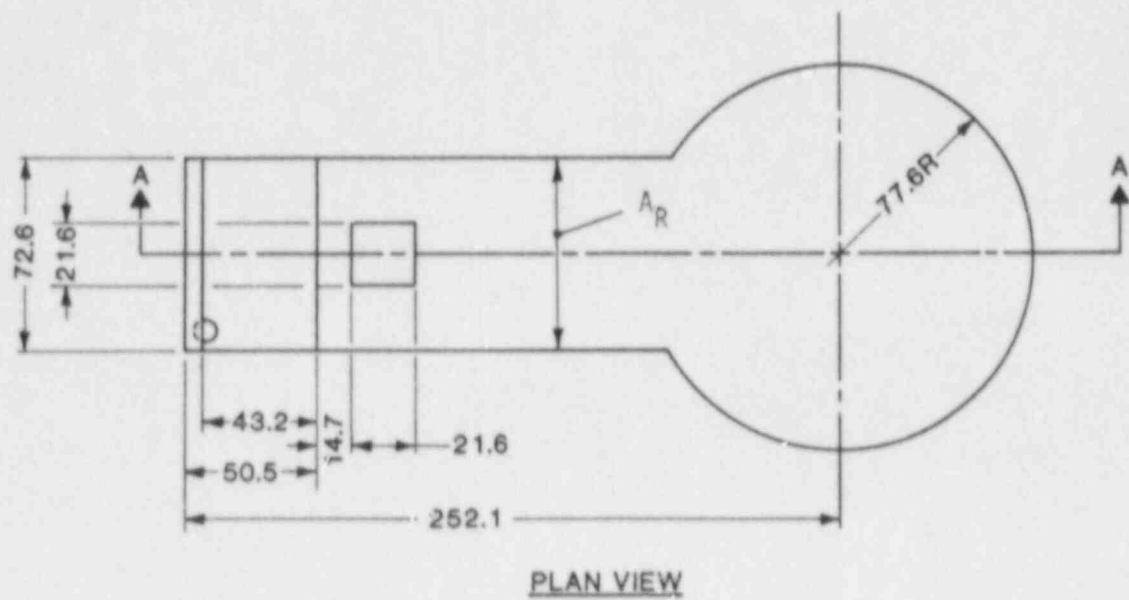


Figure 6(b) Schematic of the Surry Cavity Model
 All dimensions are in mm. $A_g = 0.00716 \text{ m}^2$

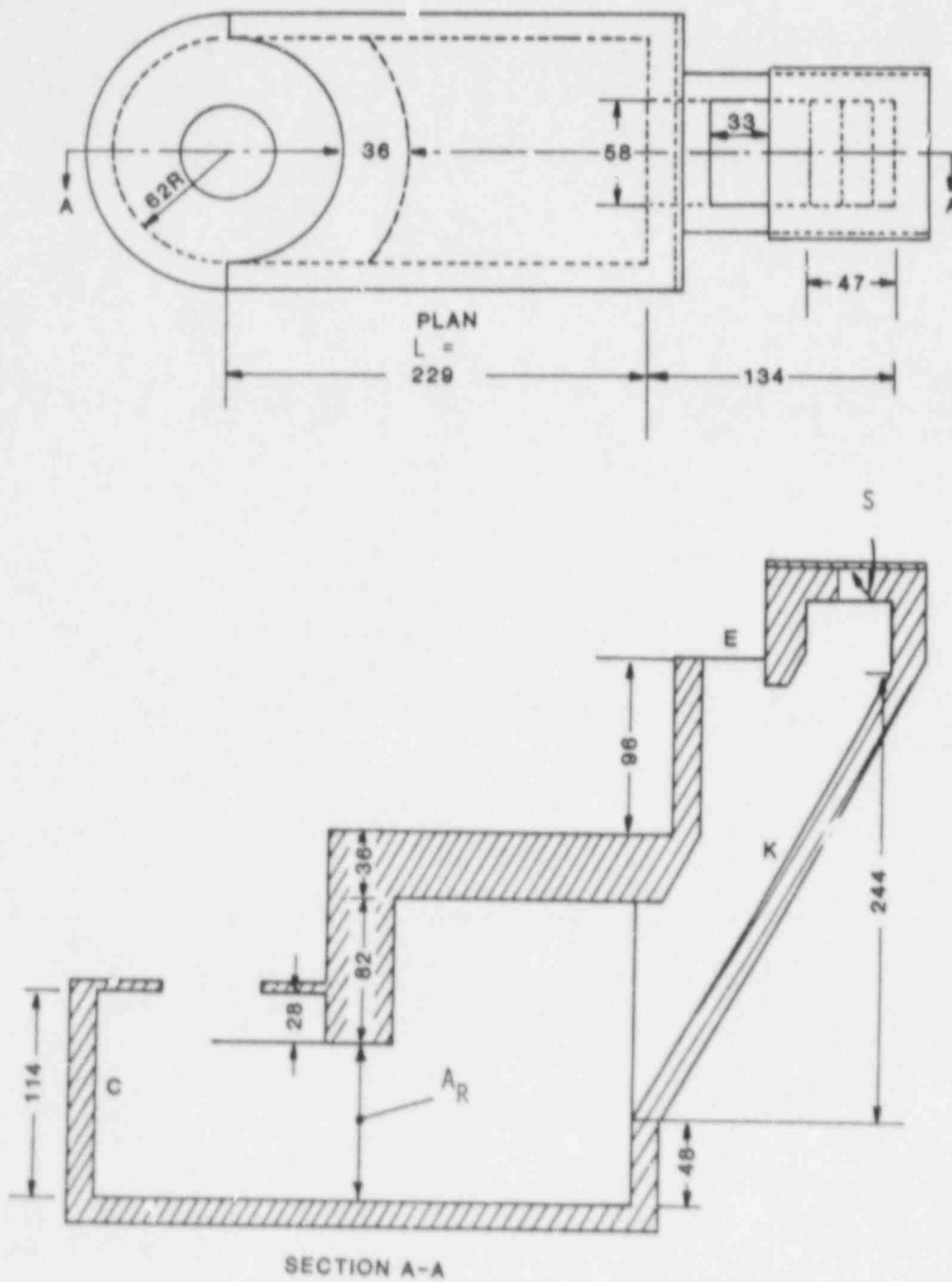


Figure 6(c) Schematic of the Watts Bar Cavity Model
 All dimensions are in mm. $A_R = 0.0106 \text{ m}^2$

Table 5. Experimental Parameters for Debris Dispersion Tests

Run #	Case	Melt Simulant	Mass of Melt Simulant (kg)	T _L (K)	V _o × 10 ² (m ³)	P _o (MPa)	T _o (K)	Diameter of Orifice* (mm)
(a) Cavity Model: Zion								
Z-1	20	Water	0.195	300	0.621	5.27	306	7.14
Z-2	20	Water	0.194	300	0.621	5.27	307	7.14
Z-3	19	Water	0.193	300	0.621	2.66	305	9.53
(b) Cavity Model: Surry								
S-1	8	Water	0.186	300	0.622	3.8	305	9.53
S-3	30	Wood's Metal	1.72	451	0.622	5.27	373	11.51
S-4	33	Wood's Metal	1.747	453	0.622	4.41	374	11.51
S-5	32	Water	0.186	299	0.622	5.27	306	6.71
S-6**	39	Wood's Metal	1.753	456	0.926	5.27	374	11.51
(c) Cavity Model: Watts Bar								
WB-1	34	Water	0.192	300	0.621	5.27	306	7.54
WB-2	36	Water	0.208	301	0.924	5.27	308	7.54
WB-3	36	Water	0.198	304	0.925	5.27	309	7.54
WB-4	35	Wood's Metal	1.75	457	0.622	5.27	378	11.51
WB-7	35	Wood's Metal	1.751	456	0.622	5.27	375	11.51
WB-8	37	Wood's Metal	1.753	456	0.926	5.27	377	11.51
*Opening through which melt simulant and the gas are discharged into the cavity.								
**For these runs, helium was used as the blowdown gas, all other runs used nitrogen as the blowdown gas.								

4. EXPERIMENTAL RESULTS

4.1 Results for the Zion Reactor Cavity Model

Table 6 shows the results of debris dispersal experiments performed with the Zion cavity model. Although by now it is well accepted that the Zion cavity is dispersive in nature (see, e.g. Ref. [3]), we present these results mainly for the sake of completeness and to show the values of various dimensionless parameters. As we can see from this table, some of the dimensionless groups are very well matched between the experiments and the full scale, while others are very different. A complete discussion of the interpretation of the debris dispersal results, in light of the values of these dimensionless groups, will be presented in Chapter 5. It should be noted that for the experiments with the Zion cavity model we have thus far used only water as the melt simulant. Experiments using molten Wood's metal as the melt simulant will be performed in the near future.

From the high-speed movies taken during the debris dispersal experiments, we make the following general observations. The experiment progresses in two stages. In the first phase, a jet of melt-simulant is directed towards the cavity floor. This is immediately followed by the blowdown of gas into the cavity. During the first phase we observe the melt simulant to spread along the floor of the cavity, with some fraction splashing in various directions. Wherever this outward moving melt simulant (film) encounters a vertical wall, it climbs up the walls. Therefore, by the time the gas injection begins, the melt-simulant is still observed to be in motion and along the various walls (and floor) of the cavity. In other words, no pool of melt simulant is observed to form on the floor of the cavity model before or during the gas blowdown phase. The above flow features were also observed during experiments with the Surry and the Watts Bar cavity models.

Figure 7 shows a schematic of the observed flow field within the Zion cavity model during the gas blowdown process for experiments where water was used as the melt simulant. We observe the gas undergoing recirculation within the cylindrical portion of the cavity (D). The gas, which is moving upward along the cylindrical walls, presumably entrains water droplets from the water film on these walls. This mixture of gas and water droplets then moves along the keyway and ultimately out of the cavity. The flow is observed to be highly turbulent everywhere. The entrainment or re-entrainment of water droplets presumably also takes place from other walls (or floor) of the cavity model. The high-speed movies of the debris dispersal process also show that before the beginning of the gas blowdown, some fraction of the melt simulant exits the cavity via the inclined keyway under its own momentum. While we have not yet made measurements of this fraction of melt simulant that leaves the cavity model under its own momentum, we estimate this fraction to be small (of the order of 20%).

4.2 Results for the Surry Cavity Model

Table 7 shows the results of the debris dispersal experiments for the Surry cavity model. We note that the observed fraction of dispersed debris from the cavity model is very high. A discussion of these results is presented in Chapter 5.

Table 6. Results of Debris Dispersal Experiments and the Values of Various Dimensionless Groups for the Zion Cavity Model

	Full Scale* Base Case ZR1	Case 20	Case 19	Full Scale* ZR2	Full Scale* ZR3
Fraction Dispersed	---	0.99**	0.995	---	---
N ₁	0.018	0.025 +	0.030 +	0.0095	0.0043
N ₂	2.04x10 ⁻³	4.56x10 ⁻² +	3.71x10 ⁻² +	3.87x10 ⁻³	8.5x10 ⁻³
N ₃	8.87	26.0 +	29.0 +	6.43	4.34
N ₄	190.7	243.1 +	122.7 +	142	372
N ₅	678.7	910.1 +	732.8	1291	2838
N ₆	6.9	8.51 +	8.0	9.52	14.11
N ₇	0.80	0.51 +	0.41 +	1.53	3.36
N ₈	0.52	0.41	0.37	0.72	*1.0
N ₉	0.41	0.33	0.40	0.44	0.34
N ₁₀	0.073	0.07	0.056	0.139	0.305

(Arrows refer to comparison with the full-scale base case. See Section 5.1 for explanation.)

*See Section 3.2 and Eq. (41) for the initial conditions assumed for the full-scale cases.

**Average of two runs, see Table 5 for experimental parameters.

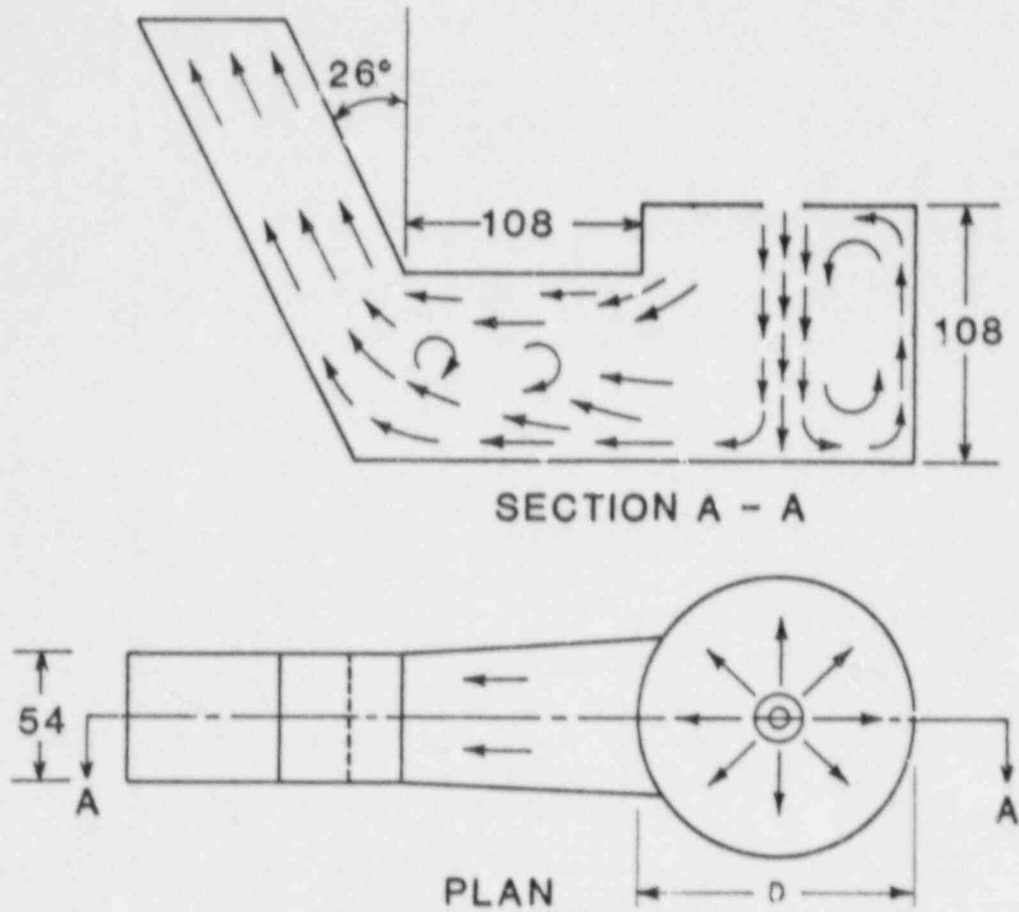


Figure 7 Schematic of Observed Gas Flow Field in the Zion Cavity Model

Table 7. Results of Debris Dispersal Experiments and the Values of Various Dimensionless Groups for the Surry Cavity Model

	Full Scale Base Case SR1	Case 8	Case 30	Case 33	Case 32	Case 9	Full Scale SR2	Full Scale SR3
Fraction Dispersed	---	0.973	0.825	0.842	1.00	0.842	---	---
N_1	0.132	0.10	1.9	2.72	0.188	11.9	0.07	0.032
N_2	0.134×10^{-3}	0.11×10^{-1}	0.517×10^{-4}	0.36×10^{-4}	0.59×10^{-2}	0.12×10^{-5}	0.255×10^{-3}	0.56×10^{-3}
N_3	10.3	49.9	132	158	68	85	7.5	5.06
N_4	621	244	308	283	336	503	462	1211
N_5	241	248	127	89	132	143	459	1009
N_6	4.1	4.6	2.4	2.1	3.4	2.6	5.67	8.41
N_7	0.59	0.14	0.57	0.4	0.074	0.57	1.12	2.47
N_8	0.45	0.22	0.44	0.37	0.16	0.43	0.62	0.92
N_9	0.34	0.36	0.27	0.28	0.33	0.17	0.37	0.29
N_{10}	0.054	0.019	0.063	0.044	0.010	0.099	0.102	0.224

See Table 5 for experimental parameters and Section 3.2 and Eq. (41) for the assumed initial conditions for the full-scale cases. Arrows refer to comparison with the full-scale base case. See Section 5.1 for explanation.

The photographs presented in Figure 8 show the trapped Wood's metal within the Surry cavity as found at the end of the debris dispersal experiment. A major fraction of the trapped Wood's metal was found along the floor [Figure 8(a)] of the cavity model. Figure 8(b) shows that some melt is also deposited on the "roof" of the keyway. In particular, we note that some of the melt deposits in this figure are in the form of elongated, downward pointing frozen drops. This, together with the fact that the melt deposited on the floor of the cavity is of approximately uniform thickness shows that Wood's metal was still in the molten state at the end of the experiment. Thus it is clear that freezing of the Wood's metal did not cause the trapping of the melt within the cavity.

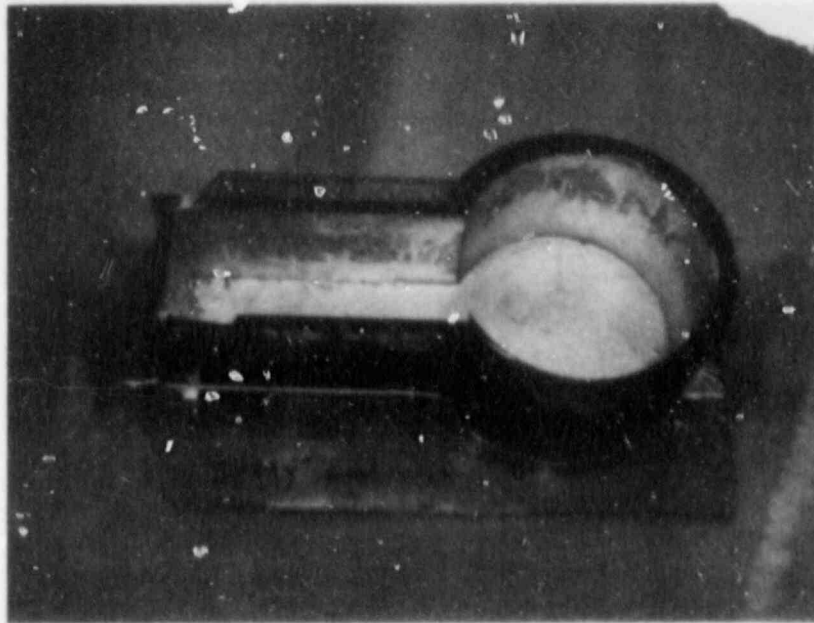
A schematic of the observed flow field within the Surry cavity model for experiments which used water as the melt simulant is shown in Figure 9. As with the Zion cavity model, here again we observe the gas to recirculate within the cylindrical portion of the cavity. The flow is highly turbulent, and we intermittently observe small regions of flow reversal near the roof of the keyway. Initially, the melt simulant is discharged only through the cavity exit C. After a short interval, however, the melt-simulant is discharged through both exits C and D.

4.3 Results for the Watts Bar Reactor Cavity

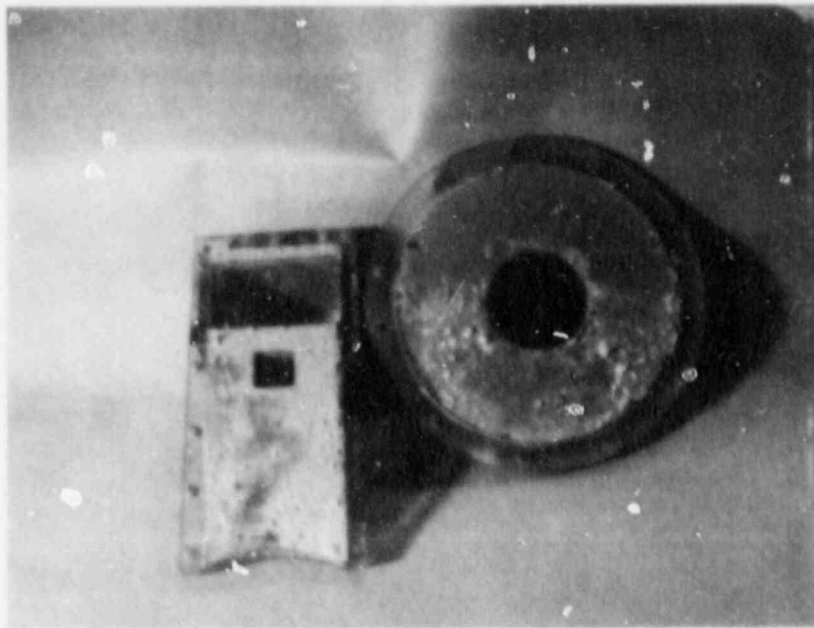
The results of the debris dispersal experiments for the Watts Bar cavity model are given in Table 8. Once again, we observe that a large fraction of the melt simulant is removed from the cavity model during the experiment. A further discussion of these results is presented in Chapter 5.

Figure 10 shows the melt disposition within the Watts Bar cavity at the end of Run WB-7. Here again we find that most of the trapped melt is on the floor of the cavity. As can be seen from Figure 10(b), some of the melt is deposited as a film along the bottom wall of the inclined keyway.

The schematic of the observed flow field within the Watts Bar cavity is shown in Figure 11. Here again we observe highly turbulent flow and a region of recirculation within the cylindrical part (C) of the cavity. However, we make two special observations for this cavity. First of all, we observe flow separation and consequently the presence of an eddy, R, within the cavity. This is obviously due to large increase in the area of cross section of the cavity in the direction of motion of the gas. Secondly, the gas-droplet mixture that is moving upwards along the keyway (K) splits up into two parts. Some of the gas-droplet mixture exits the cavity directly via path P1, and the remaining fraction moves up towards the seal table (S), then reverses direction and exits the cavity via path P2. A close observation of the flow in the neighborhood of the seal table (S) suggests that the current structure of the seal table (0.5 in. steel plate) in the Watts Bar Nuclear Plant will not survive the high-pressure melt ejection accident.



(a)



(b)

Figure 8 Trapped Wood's Metal in the Surry Cavity Model
at the End of Run S-4

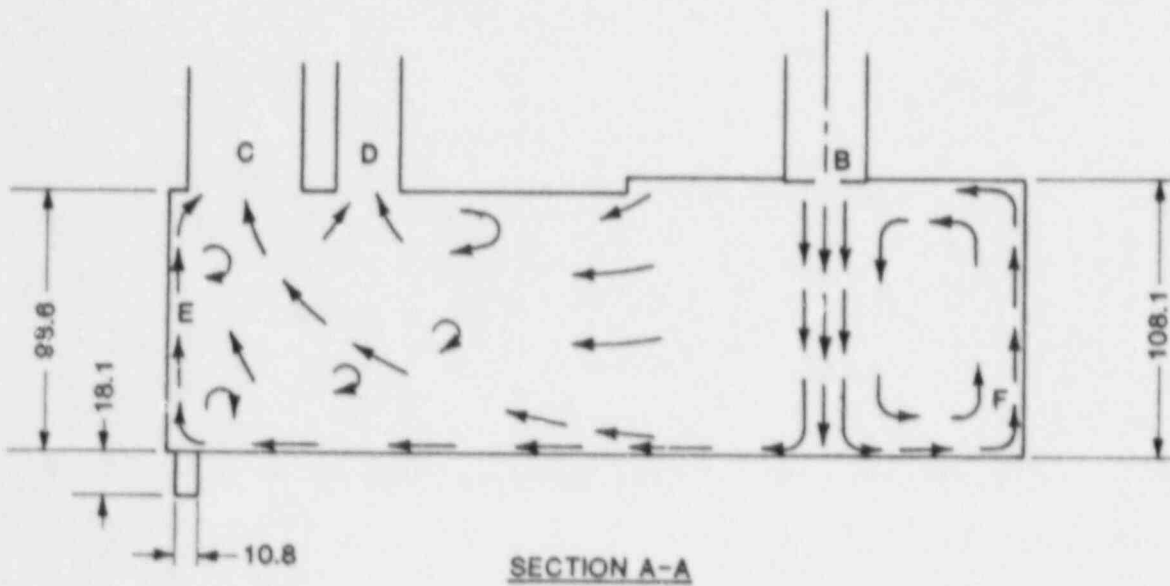
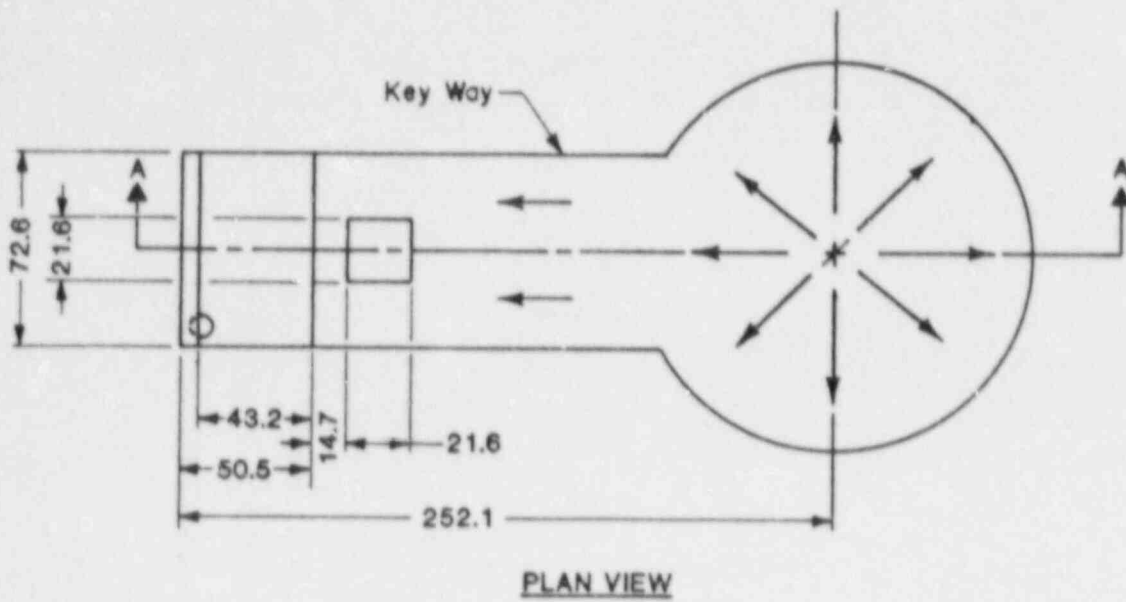
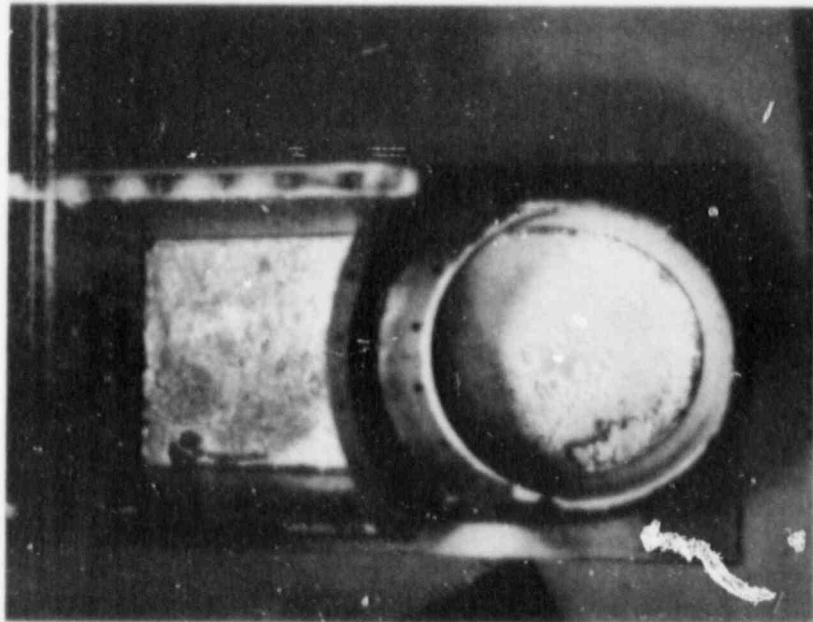


Figure 9 Schematic of Observed Gas Flow Field Within the Surry Cavity

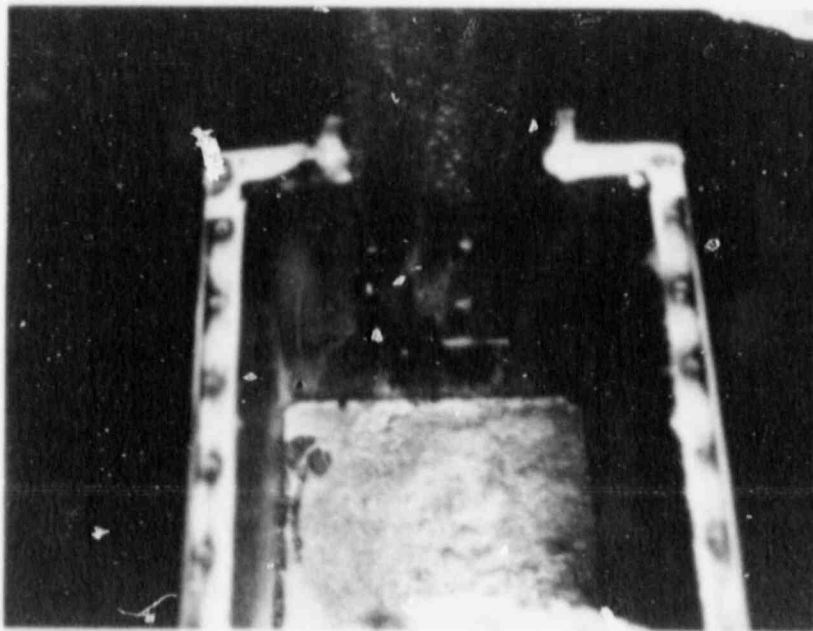
Table 8. Results of Debris Dispersal Experiments and the Values of Various Dimensionless Groups for the Watts Bar Cavity Model

	Full Scale Base Case WBR1	Case 34	Case 3b	Case 35	Case 37	Full Scale WBR2	Full Scale WBR3
Fraction Dispersed	---	0.927	0.976*	0.74*	0.823	---	---
N ₁	0.125	0.125	0.126	1.8	1.81	0.066	0.03
N ₂	1.03x10 ⁻⁴	8.96x10 ⁻³ +	8.79x10 ⁻³ +	5.4x10 ⁻⁵ +	5.4x10 ⁻⁵ +	0.196x10 ⁻³	0.43x10 ⁻³
N ₃	11.1	84.7	84.3	194	194	8.04	5.42
N ₄	91	27	40	27	40	68.1	178
N ₅	152	86	86	58	58	290	637
N ₆	3.3	2.7	2.7	1.7	1.7	4.51	6.7
N ₇	0.51	0.048	0.048	0.26	0.26	0.98	2.15
N ₈	0.42	0.13	0.13	0.30	0.30	0.58	0.86
N ₉	0.31	0.33	0.33	0.27	0.27	0.34	0.263
N ₁₀	0.047	0.007 + S	0.007 + S	0.029	0.029	0.088	0.155

*Average of two runs.
 See Table 5 for experimental parameters and Section 3.2 and Eq. (41) for the assumed initial conditions for the full-scale cases.
 Arrows refer to comparison with the full scale base case. See Section 5.1 for explanation.



(a)



(b)

Figure 10 Melt Deposition Within the Watts Bar Cavity at the End of Run WB-7

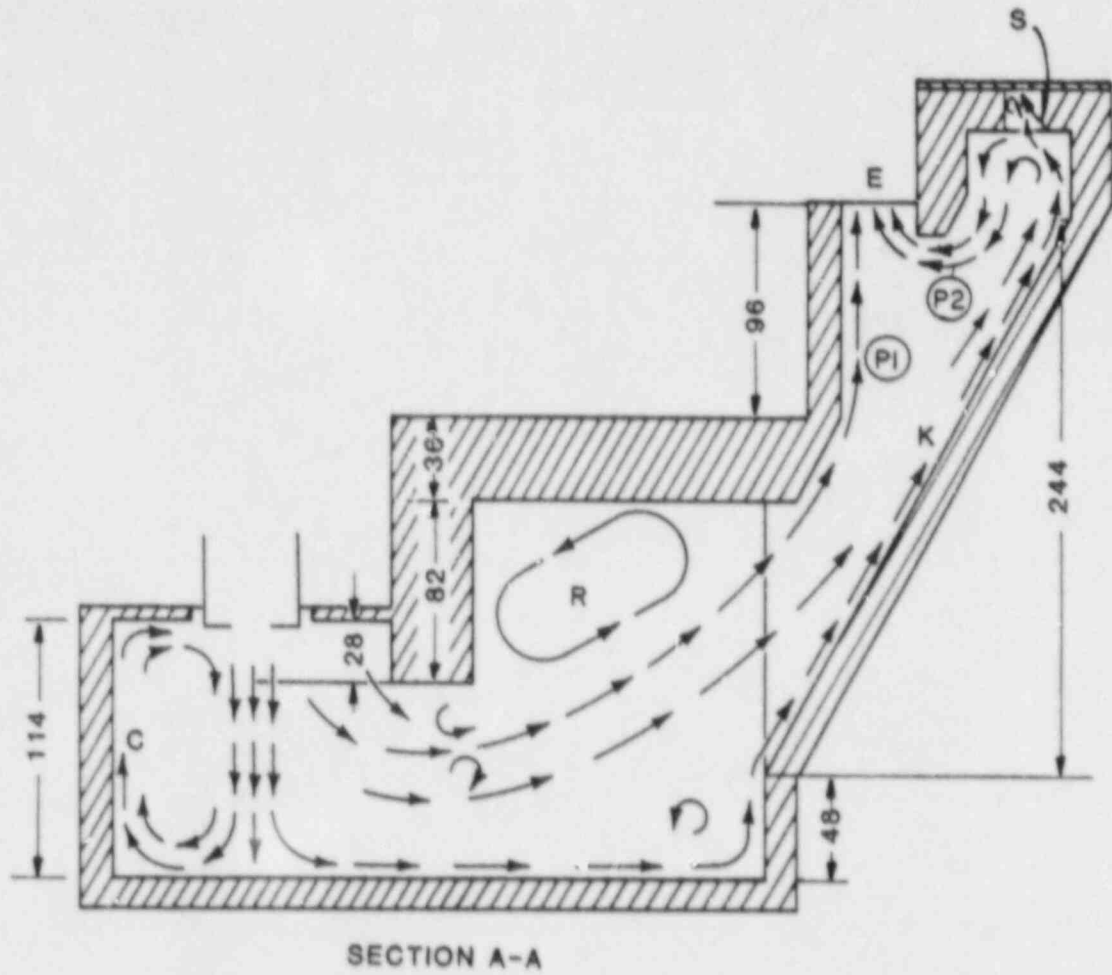


Figure 11 Schematic of the Observed Gas Flow Field Within the Watts Bar Cavity

5. DISCUSSION AND SCALING INTERPRETATION OF DISPERSAL RESULTS

5.1 Qualitative Effect of Dimensionless Groups on Debris Dispersal

The results of debris dispersal experiments for the three cavity models studied were presented in Tables 6, 7, and 8. These tables also give the values of various dimensionless numbers for all the experimental runs and the full-scale cavity for three assumed sets of initial conditions. The experiments were intended to simulate the base case full-scale conditions (Case ZR1, SR1, and WR1) as closely as possible. However, since it is impossible to match all the 10 dimensionless numbers between the experiment and the full-scale case, we must use physical arguments to interpret the experimental results. In Section 2.6 we presented a detailed discussion about the physical meaning of various dimensionless parameters. We also discussed there, the effect on debris dispersal of increasing or decreasing the various dimensionless groups. We can now use that discussion to estimate, for each of the dimensionless groups, the effect of mismatch between their values for the experiments and the full-scale base cases (ZR1, SR1, WR1) on the experimentally measured fraction of debris dispersed. This is indicated by the arrows next to the values of various dimensionless numbers for the experimental cases in Tables 6, 7, and 8.

Consider the Case 19 and N_4 in Table 6. Since N_4 is proportional to the dimensionless blowdown time, and N_4 for the experiment (122.7) is less than the value of N_4 for the full-scale base case (190.7), it is clear that because of this mismatch for the value of N_4 , the fraction of debris dispersed during the experiment can only be less than or equal to the full-scale case. This is indicated by a downward pointing arrow next to the value of N_4 . Similarly, an upward pointing arrow indicates that the experimentally measured value of the fraction of debris dispersed should be greater than or equal to the fraction of debris dispersed for the full-scale base case. The absence of an arrow indicates that, based upon our expected sensitivity of the particular dimensionless number, we think that its value is reasonably close to that of the full-scale case. The combination of an arrow and the letter "S" next to the value of a dimensionless group indicates that the measured fraction of dispersed debris should be "slightly" greater than (upward pointing arrow) or "slightly" smaller than (downward pointing arrow) the fraction of debris dispersed for the full-scale base case. For example, consider Case 32 and the group N_{10} in Table 7. Although the value of N_{10} for the experiment (0.01) is about five times lower than that of its value for the full-scale base case (0.054), based upon the expected insensitivity of N_{10} to debris dispersal (see Section 2.6), we indicate that due to this mismatch in the value of N_{10} the fraction of debris dispersed for the experiment may only be slightly smaller than that for the full scale.

From the above discussion, it is clear that if all the arrows in a given column corresponding to an experimental case are either up or down, it is easy to draw conclusions about the full-scale case. If all the arrows in a given column are downwards, then it follows that the fraction of debris dispersed for the full-scale case should be greater than or equal to the experimental value. On the other hand, if all the arrows are pointing upwards, then the experimental value of the fraction of debris dispersed is greater than or

equal to that for the full scale. For those cases where a given column has arrows in both directions, definite conclusions about the expected debris dispersal for the full-scale case may not be drawn. While comparing the values of various dimensionless groups for the experiments and the full-scale base case, one must bear in mind the fact that the full-scale values of dimensionless numbers can be very sensitive to initial conditions. Therefore, to help the reader in evaluating the closeness of the match between full-scale base case and the experimental values, we have provided in the tables of results the values of dimensionless numbers for two additional full-scale cases for each of the cavity types.

5.2 Discussion of Dispersal Results for the Zion Cavity

The values of various dimensionless numbers and the results of dispersal experiments with the Zion cavity model are given in Table 6. We note that for all the experimental cases, the arrows in each column are in both directions. Therefore, no definite conclusions about the debris dispersal for the full-scale base case can be drawn. Here we just mention that the next scheduled experiment with the Zion cavity model, which will use molten Wood's metal as the melt simulant, will have all the arrows pointing downwards. These experiments will therefore give us a lower limit on the expected debris dispersal from the full-scale Zion cavity.

However, as was pointed out in Section 4.1, based upon other experiments [1,2,3] it is now well accepted that the Zion cavity is dispersive in nature.

5.3 Discussion of Dispersal Results for the Surry Cavity

Table 7 shows the values of various dimensionless numbers and the debris dispersal results for the Surry cavity. As mentioned elsewhere, we shall only compare the values of various dimensionless groups between the experiments and the full-scale base case (SR1). The values for the remaining two full-scale cases (SR2 and SR3) are being presented only so that the reader can appreciate the sensitivity of dimensionless parameters to the assumed initial conditions. As we can see from this table some dimensionless groups (e.g., N_5 between SR1 and SR3) can change by as much as a factor of four for the full-scale case when initial conditions are changed. Since N_5 is the Mach number, and its effect on debris dispersal is not readily apparent, a question mark is placed next to the cases where it is significantly different from the full-scale case. This indicates our inability to predict the effect of mismatch in the Mach number on the measured debris dispersal. When we look at the columns represented by Cases 30 and 33, we see that all the arrows are pointing downwards. This implies that the measured fraction of debris dispersed is less than or equal to the fraction of debris dispersed for the full-scale base case. In other words, we conclude that for the full-scale Surry cavity, at least 84% of the debris will be ejected out of the cavity if the initial accident conditions are the same as assumed here. We note that for the experiment corresponding to Case 39, helium was used as the blow-down gas, and for all the experiments corresponding to Case 30, 33, and 39, molten Wood's metal was used as the melt simulant.

5.4 Discussion of Dispersal Results for the Watts Bar Cavity

The results for the Watts Bar cavity model are given in Table 8. Here we note that for the columns corresponding to Cases 35 and 37, all the arrows are pointing downwards. Therefore, we conclude that for the full-scale Watts Bar cavity, at least 82% of the debris will be ejected out of the cavity if the initial accident conditions are the same as assumed here. Furthermore, if we compare Cases 35 and 37, we note that the only dimensionless number that is different for these two cases is the group N_4 , which is proportional to dimensionless blowdown time. In agreement with our earlier arguments, we observe that the fraction of debris dispersed does indeed increase with increasing N_4 .

6. SUMMARY AND CONCLUSIONS

This report describes and presents the results of a scoping experimental study of the "extent of molten debris dispersal" from PWR reactor cavities under conditions of high-pressure melt ejection (primary system pressure approximately 1000 psia and vessel hole diameter roughly 0.4 m diameter). The experiments were conducted using scale models of the reactor cavities and were designed to employ low-temperature melt simulants. As a consequence, the experimental program was developed in conjunction with a parallel scaling analysis which is based upon phenomenological modeling of the relevant physical processes which are thought to occur within a full-scale reactor cavity under accident conditions. The experimental apparatus and method are described and experimental results presented. The phenomenological modeling and the derivation of the scaling relationships are described. A methodology based upon the scaling analysis is presented which is employed to extrapolate the experimental results for the "debris dispersal fraction" to accident conditions.

Three "representative" reactor cavities were selected: Zion, Surry and Watts Bar. An experimental apparatus was constructed to simulate the process of melt dispersal from reactor cavities during high-pressure melt ejection. The cavities were constructed to provide 1/42-nd scale simulations of the prototypic cavities and were fabricated of transparent materials to enable visual observations to be made of the flow processes within the cavities. Water and Wood's metal were employed as the low-temperature melt simulants while nitrogen and helium were used to simulate the high-pressure primary system steam (prototypic) blowdown gas. A measured quantity of melt simulant, followed immediately by blowdown gas, was injected into the cavity. The quantity of melt remaining in the cavity following the gas blowdown was measured, thus permitting calculation of the "fraction of melt dispersed" from the cavity for the given set of initial conditions. High-speed motion pictures of the cavity dispersal phenomena were recorded, from which flow patterns within the cavity were deduced.

The high-speed movies of the cavity interactions reveal a complex, multi-dimensional dispersed flow configuration within the cavity models. The melt simulant enters the cavity through an orifice in a jet configuration, whereupon the jet strikes the cavity floor and apparently distributes itself along the walls of the cavity model, all under its own momentum. Gas follows the liquid into the cavity and subsequently appears to entrain and fragment the liquid into droplets, creating a dispersed droplet flow regime within the model. The droplets are transported out of the cavity by the flowing gas.

The above qualitative observations form the conceptual basis for development of the phenomenological model of reactor cavity phenomena. This model is then applied to the scaling analysis from which the scaling relationships are derived. The model presumes the existence of a "dispersed annular-flow" regime within the reactor cavity, where droplets are dispersed in a gas core region and a liquid film is presumed to exist on the walls of the cavity. Eulerian, unsteady, one-dimensional mass, momentum and energy equations are written for each phase. Liquid temperature is assumed constant and chemical reaction between phases is not considered. Simplified constitutive relations for interfacial forces, heat transfer and entrainment are proposed. These

equations, together with the appropriate initial and boundary conditions are non-dimensionalized using reference parameters for the basic variables. This process leads to definition of eleven dimensionless parameters which characterize the debris dispersal process in the experiments. A physical interpretation of the parameters is provided in order to guide their use in scaling of the experimental results to prototypic accident conditions.

A range of initial accident conditions is defined for each of the three plants considered and a range of magnitudes of the eleven scaling parameters are calculated for each. It is shown that it is not, in general, possible to precisely match the values of the prototypic and experimental scaling parameters. The experiments reported here are performed at low temperature. As a consequence, the gas phase acceleration effects of droplet-gas heat transfer cannot be precisely simulated. An approximate method of overcoming this difficulty is employed, which relies on the assumption that the melt and steam reach thermal equilibrium very quickly within the cavity. It is further argued, on the basis of physical interpretation of the scaling parameters and with the aid of engineering judgment, that the values of the scaling parameters could be adjusted experimentally so as to provide "melt dispersal fraction" data which underestimate the extent of melt dispersal from full-scale reactor cavities under accident conditions. With the experimental scaling parameters chosen in this way the "melt dispersal fraction" data obtained using Wood's metal as the melt simulant are believed to underestimate the extent of melt dispersal under high-pressure accident conditions. Thus, if an experiment designed to simulate a high-pressure melt ejection accident led to measurement of dispersal of, for example, 80% of the melt injected into the cavity, then the interpretation of this result is that, under accident conditions, greater than 80% of the melt would be ejected from the reactor cavity. Only those experiments which could be interpreted in this way are used for the purpose of estimation of the extent of melt dispersal. For this reason, the water experiments performed here were not used for this purpose.

The experiments performed thus far with the Zion cavity were performed using water as melt simulant. Based upon the above arguments, therefore, we cannot make any judgements of the extent of melt dispersal for this system. It is noted that experiments performed elsewhere [2,3] suggest that melt ejection from the Zion reactor cavity would be nearly complete under conditions of high-pressure melt ejection. This conclusion will be verified in additional planned experiments using Wood's metal as the melt simulant. Experiments with both the Surry and Watts bar cavities, together with the scaling arguments, suggest that melt dispersal will also be nearly complete (in excess of 80%) under high-pressure melt ejection conditions.

The motion pictures of the flow patterns in the Watts Bar cavity suggest that the high-temperature dispersed melt flows through the cavity and up the inclined keyway where the flow is observed to split into two parts. One of the two resulting flow streams moves towards the seal table where the flow reverses direction and finally exits the cavity. The seal table room is covered with a steel plate which would be exposed to the high-temperature (e.g. 2500K) molten debris. It has been suggested [15] that this cover plate could fail during the time of melt ejection from the cavity, leading to transport of melt into the seal table room where contact of the melt with the containment liner could occur. Meltthrough of this liner would effectively imply

a breach of containment and "early" availability of a leakage path for fission products to the atmosphere. It is recommended that the scenario of the seal table cover plate failure during high-pressure melt ejection accidents be closely scrutinized.

The experimental results, along with the interpretation based upon the scaling analysis, suggest that the three reactor cavities studied here, i.e., Zion, Surry and Watts Bar, would retain little, if any, of the melt ejected into them from the reactor vessel following the high-pressure steam blowdown which would follow vessel failure and melt release. It is suggested that these conclusions be verified with experiments at larger scale using high-temperature melt simulant materials.

REFERENCES

1. Spencer, B.W., M. Bengis, S. Baronowsky, and J.J. Sienicki (1982), "Sweepout Thresholds in Reactor Cavity Interactions," ANL/LWR/SAF 82-1, Argonne National Laboratory.
2. Spencer, B.W., D. Kilsdonk, and J.J. Sienicki (1983), "Hydrodynamics Aspects of Ex-Vessel Debris Dispersal in Zion-Type Containment Design." ANL/LWR/SAF 83-1, Argonne National Laboratory.
3. Tarbell, W.W., M. Pilch, J.E. Brockmann, J.W. Ross, and D.W. Gilbert (1986), "Pressurized Melt Ejection into Scaled Reactor Cavities," NUREG/CR-4512, SAND86-0153.
4. Tutu, N.K., et al., Thermal Hydraulic Reactor Safety Experiments, Ch. 3 in Safety Research Programs Sponsored by the Office of Nuclear Regulatory Research, Quarterly Progress Report, April 1-June 30, 1986, compiled by Allen J. Weiss, NUREG/CR-2331, BNL-NUREG-51454, Vol. 6, No. 2, 1986.
5. Moody, F.J., "A Systematic Procedure for Scale Modeling Problems in Unsteady Fluid Mechanics," Preliminary Report, Nuclear Energy Division, General Electric Company, San Jose, CA, June 1976.
6. Wallis, G.B. (1970), "Annular Two-Phase Flow, Part 1: A Simple Theory," Journal of Basic Engineering, ASME, Vol. 92, pp. 59-72.
7. Bergeles, A.E., et al., "Two-Phase Flow and Heat Transfer in the Power and Process Industries," Hemisphere Publishing Corporation, 1971, Hewitt, G.F., "Annular Flow," pp. 163-166, J.M. Delhaye, "Two-Phase Flow Patterns," pp. 31-33.
8. Pilch, M., C.A. Erdman, and A.B. Reynolds, "Acceleration Induced Fragmentation of Liquid Drops," NUREG/CR-2247, 1981.
9. Kreith, F., "Principles of Heat Transfer," International Textbook Company, 1966, pp. 374-376, 414-415.
10. Ishii, M. and M.A. Grolmes, "Inception Criteria for Droplet Entrainment in Two-Phase Concurrent Film Flow," AIChE Journal, Vol. 21, No. 2, 1975, pp. 308-317.
11. IDCOR, "Technical Support for Issue Resolution," Technical Report 85.2, Fauske & Associates, Inc., Burr Ridge, IL, July 1985.
12. Lee, T.M., "Uncertainty Paper on High-Pressure Melt Ejection (Direct Containment Heating), December 1986, U.S.N.R.C., Washington, DC.

13. Pilch, M. and Tarbell, W.W., "High-Pressure Ejection of Melt from a Reactor Pressure Vessel - The Discharge Phase," NUREG/CR-4383, SAND85-0012, 1985.
14. Containment Loads Working Group, "Estimates of Early Containment Loads from Core Melt Accidents," NUREG-1079, 1985.
15. Pilch, M., et al., "High-Pressure Melt Ejection and Direct Containment Heating in Ice Condenser Containments," presented at the Int. ANS/ENS Topical Meeting on Operability of Nuclear Power Systems in Normal and Adverse Environments, October 1, 1986 (SAND86-2141C).

NRC FORM 335 <small>(11-81)</small>		U.S. NUCLEAR REGULATORY COMMISSION BIBLIOGRAPHIC DATA SHEET		1. REPORT NUMBER (Assigned by DOC) NUREG/CR-5146 BNL-NUREG-52147	
4. TITLE AND SUBTITLE (Add Volume No., if appropriate) Debris Dispersal from Reactor Cavities During High-Pressure Melt Ejection Accident Scenarios		2. (Leave blank)		3. RECIPIENT'S ACCESSION NO.	
7. AUTHOR(S) N. K. Tutu, T. Ginsberg, C. Finfrock, J. Klages, and C. E. Schwarz		5. DATE REPORT COMPLETED MONTH September YEAR 1987		6. DATE REPORT ISSUED MONTH July YEAR 1988	
9. PERFORMING ORGANIZATION NAME AND MAILING ADDRESS (Include Zip Code) Department of Nuclear Energy Brookhaven National Laboratory Upton, NY 11973		6. (Leave blank)		8. (Leave blank)	
17. SPONSORING ORGANIZATION NAME AND MAILING ADDRESS (Include Zip Code) U.S. Nuclear Regulatory Commission Office of Nuclear Regulatory Research Washington, DC 20555		10. PROJECT/TASK/WORK UNIT NO.		11. FIN NO. A-3024	
13. TYPE OF REPORT Form 1		PERIOD COVERED (Inclusive dates) March 1986 to September 1987			
15. SUPPLEMENTARY NOTES		14. (Leave blank)			
16. ABSTRACT (200 words or less) <p>This report presents the results of a scoping experimental study of the "extent of molten debris dispersal" from PWR reactor cavities under direct containment heating conditions. Simulated high-pressure melt ejection experiments were conducted using 1/42nd-scale models of reactor cavities and were designed to employ low-temperature melt simulants. Three "representative" reactor cavities were selected: Zion, Surry, and Watts Bar. A scaling analysis of the debris dispersal phenomena was carried out and was employed to extrapolate the experimental results for "debris dispersal fraction" to accident conditions. The experimental results, along with the interpretation based upon the scaling analysis, suggest that the three reactor cavities studied here, i.e., Zion, Surry, and Watts Bar, would retain little, if any, of the melt ejected into them from the reactor vessel following the high-pressure steam blowdown which would follow vessel failure and melt release.</p>					
17. KEY WORDS AND DOCUMENT ANALYSIS Debris Dispersal, Melt Dispersal, High-Pressure Melt Ejection, Direct Containment Heating, Reactor Cavities		17a. DESCRIPTORS			
17b. IDENTIFIERS, OPEN ENDED TERMS					
18. AVAILABILITY STATEMENT		19. SECURITY CLASS (This report)		21. NO. OF PAGES	
		20. SECURITY CLASS (This page)		22. PRICE	

120555139217 1 1A1R2
US NRC-OARM-ADM
DIV FOIA & PUBLICATIONS SVCS
RES-PDR NUREG
P-210
WASHINGTON DC 20555